Pedro Afonso Magalhães Centeno

Licenciado em Ciências de Engenharia de Micro e Nanotecnologia

Self-cleaned Solar Cells with Super-Hydrophobic Photonic Nano-structures

Dissertação para obtenção do Grau de Mestre em
Engenharia de Micro e Nanotecnologias

Orientador:	Prof. Dr. Manuel João de Moura Dias Mendes, Post-Doc Fellow and Invited Assistant Professor, FCT-UNL
Co-orientador:	Prof. Dr. Hugo Manuel Brito Águas, Associate Professor, FCT-UNL

Júri:

Presidente:	Prof. Doutor Rodrigo Fernão Paiva Martins
Arguente:	Prof. Doutora Joana Dória Vaz Pinto
Vogal:	Prof. Doutor Manuel João de Moura Dias Mendes

FACULDADE DE CIÊNCIAS E TECNOLOGIA
UNIVERSIDADE NOVA DE LISBOA

Outubro 2018

Self-cleaned Solar Cells with Super-Hydrophobic Photonic Nano-structures

Acknowledgement

Em primeiro lugar, gostaria de agradecer à Professora Dra. Elvira Fortunato e ao Professor Dr. Rodrigo Martins pela criação e desenvolvimento do curso de Micro e Nanotecnologias e pelas condições oferecidas no CENIMAT|i3N e no CEMOP.

Gostaria de agradecer ao meu orientador, Professor Dr. Manuel Mendes e ao meu co-orientador, Professor Dr. Hugo Águas, pela introdução do tema, o qual se revelou incrivelmente interessante e estimulante, pelo apoio com os problemas que fui apresentando e, especialmente, pela paciência e disponibilidade prestados ao longo deste tempo.

À Olalla, pelas formações a equipamentos e pelos conselhos.

À Alexandra Gonçalves e à Sónia Pereira pela formação em equipamentos e, especialmente, pelo fornecimento de material (mesmo a des-horas).

Um agradecimento sentido à Professora Marta Corvo, pelo apoio técnico na sala de RMN (desculpe qualquer coisinha).

À Professora Helena Godinho pela introdução à bíblia de *de Gennes*.

À Professora Rita Branquinho por toda a ajuda prestada, por me dar formação em vários equipamentos e, sobretudo, pela paciência infinita.

Ao Tomás por me fazer uns quantos testes no AFM e pelos almoços ali pela cova e tal e à Daniela Gomes pelas sessões de SEM.

Ao Tiago Mateus por me orientar com as medidas das células solares e pela disponibilidade em tudo.

Ao Jonas Deuermeier pelas sessões de XPS e por toda a ajuda, que foi preciosa.

À Ana Santa, à Cátia, à Inês Martins e ao Trigo por me acompanharem à càmara limpa e por toda a ajuda que me deram. Cátia e Inês, sem vocês o parileno não seria o mesmo.

À Jenny Boane e ao João Luís por tudo.

Obrigado a toda a gente que, não estando no ambiente de trabalho, me estimularam para dar o melhor, sempre.

E um obrigado especial à Carolina Pitágoras pela revisão tão such nice e pelo resto.

Abstract

This work has investigated the light scattering effect and self-cleaning (*i.e.* water hydrophobicity) properties of various micro/nano-structured front coatings for solar energy applications. This was done through enhancement of surface texturing, following a colloidal lithography methodology, which comprised the reactive ion etching of the material with a pre-deposited mask of a self-assembled monolayer of polystyrene microspheres. This process culminated in the formation of a surface patterned with micro structures.

Experimentally, the maximum water contact angles obtained were 140° and 167°, for PET and parylene-C materials, respectively. The results of scanning electron microscopy suggest the wettability properties change due to variations in surface roughness at micro and nano scales. Then, through x-ray photoelectron spectroscopy analysis, that change was associated with variations in surface chemistry. Droplet state transition from Wenzel state to Cassie-Baxter state for parylene was analytically demonstrated through examination of water advancing and receding contact angles.

It was observed that increasing plasma exposure results in an increase of reflectance and in a slight decrease of total transmittance. However, diffuse transmittance increased from 5% and 2% to above 60% for PET and parylene, respectively, which reveals potential for light trapping (via optical path length amplification). These changes are directly related to surface roughness modification and they intensify with colloidal lithography.

For proof-of-concept, a-Si solar cells were fabricated in superstrate (p-i-n) and substrate (n-i-p) configurations to evaluate the performance of the textured parylene as a photonic-structured encapsulant. The measured devices showed a photocurrent (J_{SC}) enhancement up to 16%, in the substrate configuration, due to the light trapping effects of the photonic-structured parylene. In addition, the structured parylene layer also acted as a pronounced superhydrophobic surface which strengthens the device robustness in outdoor operation.

Resumo

Este trabalho investigou as propriedades de dispersão de luz e auto-limpeza (*i.e.* hidrofobicidade da água) de vários revestimentos frontais micro/nano-estruturados para aplicação em energia solar. Isto foi realizado através da otimização da texturização de superfície, seguindo uma metodologia de litografia coloidal, constituída pela erosão reativa iónica do material com recurso a uma máscara composta por uma monocamada de microesferas de polistireno auto-dispostas. Este processo culminou na formação de uma superfície modelada com microestruturas.

Experimentalmente, os ângulos de contato máximos da água obtidos foram 140° e 167°, para os materiais PET e parileno-C, respectivamente. Os resultados da microscopia eletrónica de varredura sugerem que as propriedades de molhabilidade mudam devido a variações na rugosidade superficial às micro- e nano-escalas. Assim, através da análise de espectroscopia de fotoeletrões de raio-X, essa mudança foi associada a variações químicas da superfície. Foi ainda analiticamente demonstrado, através do estudo dos ângulos de contato de avanço e de recuo em parileno, um estado de transição entre os estados de Wenzel e de Cassie-Baxter.

Observou-se que o aumento do tempo do tratamento de plasma resulta no aumento da reflectância e na ligeira diminuição da transmitância total. No entanto, a transmitância difusa aumentou de 5% e 2% para valores acima de 60% para PET e parileno, respectivamente, o que revela potencial para difusão de luz (pela amplificação do comprimento do caminho óptico). Estas alterações estão diretamente relacionadas com a modificação da rugosidade superficial e são intensificadas com o uso de litografia coloidal.

Para prova de conceito, foram fabricadas células solares de a-Si em configurações de superstrato (p-i-n) e substrato (n-i-p) para avaliar o desempenho do parileno texturizado como um encapsulante com propriedades fotónicas. As células testadas revelaram um aumento de fotocorrente (J_{SC}) de 16%, na configuração de substrato, devido aos efeitos de aprisionamento de luz do parileno com estruturas fotónicas. Para além disto, a camada de parileno estruturado atuou também como uma superfície superhidrofóbica que fortalece a robustez do dispositivo em funcionamento no exterior.

Abbreviations

ACA – Advancing CA

AFM – Atomic Force Microscopy

a-Si - Amorphous Silicon

CA – Contact Angle

CEMOP - Center of Excellence in Microelectronics Optoelectronics and Processes

CL – Colloidal Lithography

COS – Consecutive-O_2-SF_6

CVD – Chemical Vapor Deposition

EDS – Energy Dispersive Spectroscopy

EQE – External Quantum Efficiency

FWHM – Full-width-half-maximum

IPA – 2-propanol

I-V – current-voltage

ITO – Indium Tin Oxide

LED – Light emitting diode

LB – Langmuir-Blodgett

PECVD – Plasma enhanced chemical vapor deposition

PEN - Polyethylene naphthalate

PET - Polyethylene terephthalate

PS – Polystyrene

PV – Photovoltaic

RCA – Receding CA

RF – Radio Frequency

RIE – Reactive Ion Etching

R_D – Diffuse Reflectance

R_S – Specular Reflectance

R_T – Total Reflectance

SEM – Scanning Electron Microscopy

T_D – Diffuse Transmittance

T_S – Specular Transmittance

T_T – Total Transmittance

UV-VIS-NIR – Ultraviolet-Visible-Near-infrared

XPS – X-Ray Photoelectron Spectroscopy

Symbols

f_{SL} – fraction of solid-liquid contact interface

η – Efficiency

R_f – Roughness Factor

θ – Contact Angle

γ – Surface Tension

J_{SC} – Short Circuit Current Density

FF – Fill Factor

V_{OC} – Open Circuit Voltage

Table of Contents

List of Tables

List of Figures

Motivation and Objectives

Accumulation of dust, airborne dirt, snow and other particles on the solar panel surface, causes solar cells to capture less sun-light and degrade faster (e.g. via hot-spot formation [1]), affecting the conversion of light into electricity. This might not look problematic if thinking about a single solar panel. However, when multiplied by the thousands or millions of solar panels in a solar installation, it becomes very costly, requiring periodical maintenance.

On the other hand, with increasing interest in thin-film photovoltaics, light trapping effects became extremely important. As the thickness of the absorbing layer is reduced to hundreds of nanometers, absorption of longer wavelengths (NIR) is compromised. A very efficient approach to resolve this problem is the introduction of light scattering. This effect increases the optical path length inside the absorbing layer, enabling the harnessing of radiation with longer wavelengths.

The main focus of this thesis is, therefore, the development of surfaces with self-cleaning properties which also possess light scattering capability. This will be accomplished by following a simple surface-patterning methodology based on colloidal lithography (CL), enabling low production costs since it does not require expensive specialized equipment as in conventional photolithography. The CL methodology comprises three fundamental stages. [2] The first is the deposition of a self-assembled hexagonal compact monolayer of polystyrene (PS) microspheres on a given material's surface through Langmuir-Blodgett method. The second stage is the material's patterning through reactive ion etching (RIE), using the PS monolayer as physical etching mask. The last stage is the sphere removal. This process results in the formation of a surface patterned with micro-cylinders/dome-like structures, which can lead to improved self-cleaning and light scattering properties.

Initially, the deposition of PS microspheres on various surfaces will be investigated and the study of PS diameter will be conducted in order to optimize the spheres' self-assembly. These self-assembled PS monolayers will then be used as physical masks during the reactive ion etching process. In this stage various parameters will be studied in order to enhance the hydrophobicity and light scattering capability of the surfaces. This will be accomplished by fine tuning the high aspect ratio cylinder/dome-like shaped structures obtained through colloidal lithography and by the chemistry modification of the surface, specifically introducing fluorinated functional groups.

The developed surfaces will be observed through SEM and AFM in order to accurately study the influence of aspect ratio and shape of the CL-patterned features in the wetting and optical properties. Then, they will be subjected to static and dynamic contact angle (CA) measurements which will characterize the wettability (i.e. hydrophobicity properties). The optical properties will be investigated through transmittance and reflectance spectra analysis. Here, the haze factor (ratio between diffuse and total transmittance) will be studied and maximized. Surface chemistry modifications induced by plasma treatment will be analyzed through x-ray photoelectron spectroscopy. Also, the analytical comparison of the obtained CA results with two theoretical models will be presented. Finally, amorphous silicon (a-Si)

solar cells in substrate and superstrate configurations will be tested and compared with the application of a parylene layer on the cells' front and subsequent patterning following the best conditions previously investigated.

1 Introduction

1.1 Self-cleaning in solar cell technology

The power output generated by a photovoltaic (PV) solar cell is limited by the amount of irradiance that reaches it. A factor often disregarded when designing PV technology is soiling loss. [3] Due to accumulation of dust, airborne dirt (both organic and inorganic), snow and other particles on the panel surface, solar cells capture less sun light, hindering the conversion of light into electricity. This might not look problematic if thinking about a single solar panel. However, when multiplied by the thousands or millions of solar panels in a solar installation, it becomes very costly.

Studies have reported decreases in efficiency of different values throughout different periods and locations. [4]–[8] One example is the reported 10.4% and 9.7% efficiency loss in 30° and 55° tilted solar panels, respectively, in the Jazan region over the course of 16 weeks (Figure A 1). [4] Ahmad Al-Hasan has investigated both experimentally and mathematically the optical losses caused by dust deposition on the solar panels, reducing the surface transmittance up to 50%, as shown in Figure A 2. [9] An available solution to this problem is manual cleaning that includes water spraying. This approach requires the use of large quantities of water, an especially scarce resource in arid regions. Besides being energy and time-consuming, it might cause cracks on the PV panel surface from inadequate brushing. [10]

Figure 1.1.1 – Example of solar panels cleaning system.

Self-cleaning based solutions have therefore been the focus of various research teams, presenting a wide range of approaches. [10] The first is an electrostatic method (completely independent of water) by means of electrodynamic screens (EDS) that utilize high voltage to produce an electrical field that repels the dust particles; the second comprises four different mechanical techniques – brushing, air-blowing, water-blowing and ultrasonic vibration; the third is the coating technique, which consists of either superhydrophilic coatings that cause a photo-catalytic reaction which chemically breaks down the organic dirt, or superhydrophobic coatings that due to their notably low surface tension (addressed in section 1.2), allow water to easily flow down the panel "sticking" to the dust particles, thus producing the self-cleaning effect. Resorting to self-cleaning technologies, specifically through the development of textured coatings, the need for periodical maintenance automatically decreases. In turn, this lowers maintenance costs and the use of water and enables the integration of photonic structures with the ability of enhancing light trapping and anti-reflection properties of PV solar cell, further improving its efficiency. [11]

1.2 Wettability

This field has been studied since the early 19th century by researchers such as Pierre Laplace (1749-1827) and Thomas Young (1773-1829). It has a wide range of applications, including in botany, glass industry and oil recovery. The core concept in wettability is surface tension. On the one hand, if we think of an atom inside of a liquid droplet, it is bonding with its surrounding atoms, finding itself in a "balanced" state. On the other, an atom located at the surface has less cohesive interactions, thus being in an "unbalanced" and more energetic state (see Figure 1.2.1). This excess surface energy, or surface tension, γ, is the energy that must be supplied to increase the surface area by one unit. In order to minimize the surface tension, liquids naturally adjust their shape, lowering their exposed surface area . [12, pp. 1–4]

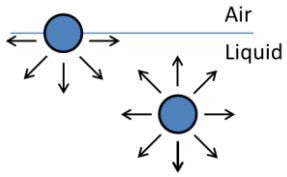

Figure 1.2.1 – Representation of the interactions on bulk and surface atoms.

When a water droplet is deposited on a solid surface, equilibrium is reached. Three interfaces are to be acknowledged: a solid-liquid interface, a liquid-air interface and a solid-air interface. The angle formed by the intersection of the solid-liquid and liquid-air interfaces (three-phase contact line) is referred to as (static) contact angle (CA), θ_0, as represented in Figure 1.2.2a. A common way to characterize a surface wettability is through its CA. If a given surface has a CA higher than 90°, the surface is hydrophobic, meaning it has a low wettability. By contrast, if the surface has a CA lower than 90°, the surface is hydrophilic and has a high wettability. Surfaces with a CA greater than 150° are superhydrophobic. The CA of a droplet on an ideal (smooth and chemically homogenous) surface is described by Thomas Young's relation [12, p. 216],

$$cos\theta_0 = \frac{\gamma_{SA} - \gamma_{SL}}{\gamma_{LA}} \tag{1.1}$$

where γ_{SA}, γ_{SL} and γ_{LA} are the surface energies of the solid-air, solid-liquid and liquid-air interfaces, respectively. Although from this equation it is expected that a single CA will be found for a given surface, in practice, the surface is neither perfectly smooth, nor homogenous. The droplet presents metastable states whose CAs usually do not correspond to the static CA described above, making this measurement unreliable. [13, p. 5,6] Before discussing how roughness and heterogeneity might influence wettability, it is important to consider the concept of dynamic CA. For a more accurate evaluation of a surface's wettability, advancing and receding contact angles (ACA, θ_A, and RCA, θ_R, respectively) were introduced. The difference between them is called CA hysteresis ($Hys = ACA - RCA$). They measure the CA of a droplet the moment before the contact line (solid-liquid interface) suffers a change. There are several ways of determining dynamic CA. [14] A very straight forward one is the tilting method, shown in Figure 1.2.2c. The ACA is measured at the front of the droplet and the RCA is measured at the back.

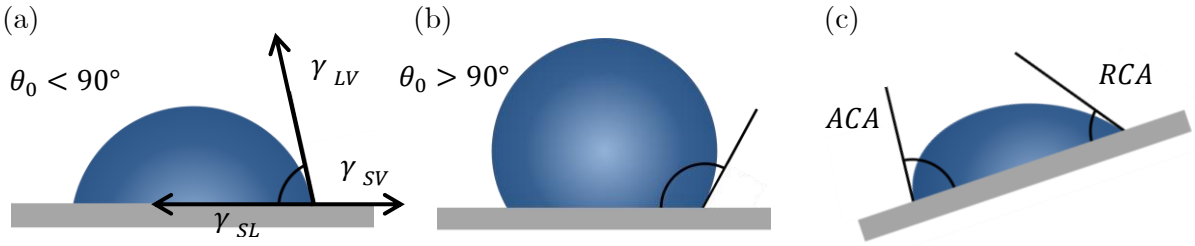

Figure 1.2.2 – Representation of (a) water droplet static CA on a hydrophilic surface and the surface energies of each interface, (b) CA on a hydrophobic surface and (c) dynamic CA w/ tilt method.

An experiment by Johnson and Dettre in 1964 [15] revealed that there is a connection between surface roughness and wettability. They measured the ACA and RCA of water droplets on wax surfaces applying heat treatments in between each measurement and successively decreasing the surface roughness. The results are presented in Figure A 3. It is evident that roughness has a direct impact on both contact angle and its CA hysteresis. One can easily distinguish two main regions. Whereas in the first region (of lower roughness) the measured CA is relatively low and the hysteresis is high, which reveals a highly adhesive behavior while still hydrophobic, in the second region (of higher roughness) the CA is extremely high and accompanied by a low hysteresis, assuming a superhydrophobic state. There is a correlation between these profoundly dissimilar behaviors and the two standard wetting models supporting this work. The first is the Wenzel model [16].It is based on the premise that the water droplet fills the full surface area, as represented in Figure 1.2.3a, in this way introducing a roughness factor, $R_f > 1$, that consists of the ratio of actual solid surface area to its flat projected area. The effective surface energies of the solid-air and solid-liquid interfaces become $R_f\gamma_{SA}$ and $R_f\gamma_{SL}$, respectively. [17] It is still assumed in this model that the *local* CA is admitted by Young's relation [Eq. (1.1)], and the apparent angle, θ^*, is given by Wenzel equation for a rough surface [16]:

$$cos\theta^* = R_f cos\theta_0 \tag{1.2}$$

In contrast with Wenzel's model, the second model, [18] – Cassie-Baxter – assumes that air is confined in spaces between the rough solid surface and liquid. It adds that there is no impregnation in these confined "air pockets", meaning the droplet is seated on a heterogeneous planar surface (Figure 1.2.3b). The fraction of solid-liquid contact interface can then be defined as $0 < f_{SL} < 1$. Likewise, the fraction of liquid-air contact interface can be defined as $(1 - f_{SL})$. The CA is given by Cassie-Baxter equation [17]:

$$cos\theta^* = R_f f_{SL} cos\theta_0 - 1 + f_{SL} \tag{1.3}$$

If impregnation occurs, $f_{SL} = 1$, i.e. the fraction of liquid-air contact interface, $(1 - f_{SL}) = 0$, equation 1.3 reduces to Wenzel's equation. Despite the binary character of both Wenzel and Cassie-Baxter models, there have been studies [17], [19]–[21] reporting the existence of a transitional wetting state between Wenzel and Cassie-Baxter states, where the droplet partially impregnates the texture while still remaining a solid-air interface (Figure 1.2.3c). In this case the droplet is no longer supported by a planar surface, increasing the solid-liquid interface area. The liquid-air interface area is dependent on the surface geometry.

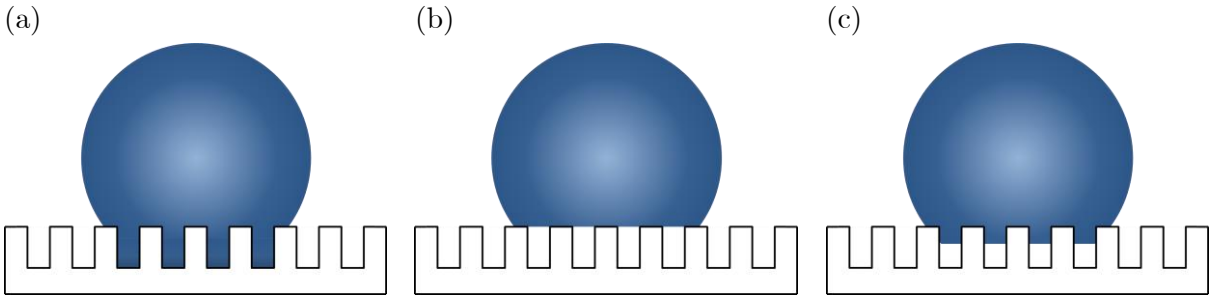

Figure 1.2.3 – Representation of the configurations described by (a) Wenzel equation, (b) Cassie-Baxter equation w/out impregnation and (c) transition state with partial impregnation.

Another way to tune the wettability of a given surface is by altering its surface chemistry. [12], [22]–[24].

Fluorine-based plasmas are a common solution for polymer's surface hydrophobization. This technique can have two effects – functionalization or polymerization. Their occurrence is related to the F/C ratio. If F/C>3, there will be no polymerization; if F/C<2, there will be polymerization of fluorocarbons on the surface. Therefore, gases like CF_4 and SF_6 do not cause polymerization, unless CH_4 is added, given that CH_4 alters the F/C ratio. Fluorination with CF_4 and SF_6 is then based on functionalization, specifically with CF, CF_2 and CF_3 functional groups. At low pressure, there is a strong dissociation of CF_4 and SF_6, enabling the formation of high density F atoms in the plasma. Although information about plasma interaction with parylene-C is limited, the literature states that, with PET, F atoms chemically interact with the surface, leading to partial substitution of the oxygen. This interaction process is nevertheless not yet fully understood. [24] Another approach towards hydrophobicity is the application of a sequential plasma treatment – an O_2 plasma treatment. This treatment presents a higher etching rate and induces the incorporation of oxygen-containing functional groups into an oxygen-free polymer [25], turning it (super)hydrophilic, followed by a SF_6 plasma that reverts the surface wettability to superhydrophobic. Reactive ion etching (RIE) is a particularly attractive approach because of its low processing temperature (ambient) and lower pressure, which promotes anisotropic etching/sputtering. RIE consists of a chemical and physical process which not only alters the surface chemistry but also realizes its texturing or patterning, depending on whether colloidal lithography is applied (This topic will be further addressed on section 1.3).

Since the discovery and study of the "Lotus" effect [26]–[28], a very interesting area is emerging within wettability studies, more specifically in the development of superhydrophobic surfaces through biomimetic approaches [17], [19] The leaves of the *Nelumbo nucifera* possess a hierarchical structure at both micro- and nano-scales (Figure A 4) which enables them to efficiently repel water and consequently any residue or contaminant on its surface. [27] This is a typical superhydrophobic behavior where there is high CA, low hysteresis (culminating in a low roll-off angle) and low adhesion. There has been a lot of recent discussion around the concept of superhydrophobicity because of the "Rose Petal" effect (SEM image in Figure A 5) and its wettability. It is a superhydrophobic surface with extreme adhesion to water, that results in a high CA and a large CA hysteresis. [17] This effect was reproduced with polystyrene nanotubes [28].

1.3 Photonic front structures

Wavelength-sized photonic structures have received tremendous interest in the context of thin-film photovoltaics (PV). Due to limitations imposed by the physical dimensions of thin-film solar cells, several light trapping and anti-reflection schemes have been emerging that have an extremely close dependence on the photonic elements. One of the main contributions for thin-film photovoltaic efficiency is the enhancement of optical path length of near-infrared (NIR) light. [29] This enhancement can be achieved through the introduction of light scattering elements on the front side of solar cells (Figure 1.3.1). The fabrication of these structures can be performed through colloidal lithography which is the preferential soft-lithography technique compatible with PV industrial manufacturing.

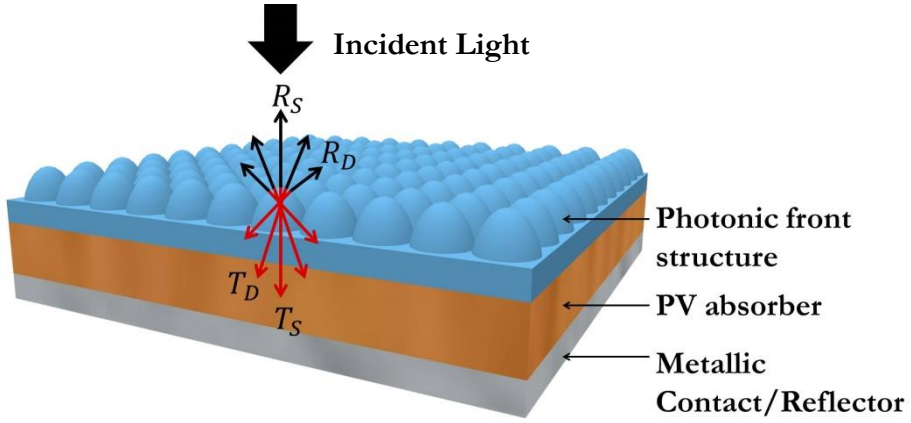

Figure 1.3.1 – Representation of front side photonic micro-domes with light scattering properties.

When an unidirectional beam strikes a medium it is simultaneously transmitted and reflected (Figure 1.3.1). The transmitted beam separates itself into two components. The first conserves the incidence direction, called specular transmittance (T_S) and the other deflects into many directions, diffuse transmittance (T_D). The sum of regular and diffuse components results in total transmittance (T_T). The same reasoning applies to reflectance, which in turn generates R_S (specular reflectance), R_D (diffuse reflectance) and R_T (total reflectance). When the photonic structures are applied in the solar cell's illuminated face, the light scattering enhancement is therefore obtained through the maximization of T_D. The factor that correlates T_D with T_T is called haze in transmittance, which is defined as:

$$Haze = T_D/T_T \tag{1.4}$$

2 Materials and Methods

Several materials were investigated for surface patterning. Glass, PEN (Polyethylene naphthalate - $(C_{14}H_{10}O_4)_n$) and PET (Polyethylene terephthalate - $(C_{10}H_8O_4)_n$) are eligible for use in superstrate device configurations (*e.g.* conventional perovskite solar cells). PEN and PET may even be integrated in the fabrication of flexible solar cells. Due to the reduced thickness and the deposition properties of parylene-C ($(C_{16}H_{14}Cl_2)_n$) (described in section 2.2), its main application is herein front encapsulation.

2.1 Substrate preparation

PET with indium-tin oxide (ITO) on one side and PEN substrates were cut to 5.0×7.0 cm in order to fit the Langmuir-Blodgett deposition well and cleaned with regular detergent. Then, in ultrasound vibration, were dipped in 2-propanol (IPA) and deionized water, sequentially.

Glass with $10.0 \times 10.0 \times 0.1$ cm was cut into 5.0×7.0 cm and cleaned with regular detergent. Then, in ultrasound vibration, was sequentially dipped in acetone, followed by IPA and finally deionized water.

2.2 Parylene-C Deposition

Parylene was deposited through vacuum chemical vapor deposition (CVD), using a PDS 2010 Labcoter 2 (Specialty Coating Systems). The process consists of four stages – According to the relation between dimer mass and parylene film thickness reported elsewhere [30] and shown in Figure B 1 (Appendix B), the appropriate amount of dimer is loaded into the vaporization chamber. Then the system creates vacuum and the dimer dichloro-di(*p*-xylylene) goes through the vaporization stage at 175 °C. The gaseous dimer enters the pyrolysis chamber, where at 690 °C it is pyrolyzed to form its monomer, chloro-*p*-xylylene, and finally polymerizes in the deposition chamber onto the glass substrate at room temperature (Figure B 2). The thickness of parylene was verified by profilometer. The glass/parylene substrate was cleaned again with detergent, IPA and deionized water sequentially.

2.3 Nano/micro-structures formation

The surface processing was performed through the use of colloidal lithography (CL), which involved 3 steps that are illustrated in Figure 2.3.2. The first step was the deposition of a self-assembled monolayer of polystyrene (PS - $(C_8H_8)_n$) microspheres on the surface of the material in question through the Langmuir-Blodgett method (Figure 2.3.1). Then, the material is patterned via reactive ion etching (RIE), with the spheres serving as physical etching mask (Figure 2.3.2b). The last step is the removal of the PS spheres with IPA in ultrasound vibration (Figure 2.3.2c).

2.3.1 PS microspheres deposition

Langmuir Blodgett developed a methodology for the formation of monolayers (Langmuir monolayers), [31] resorting to a trough based on the design by Agnes Pockels (later called the 'Langmuir-Blodgett trough'). Through his methodology, it became possible to transfer a single compact monolayer [32] from the water surface onto a given substrate by dip coating, as represented in Figure 2.3.1.

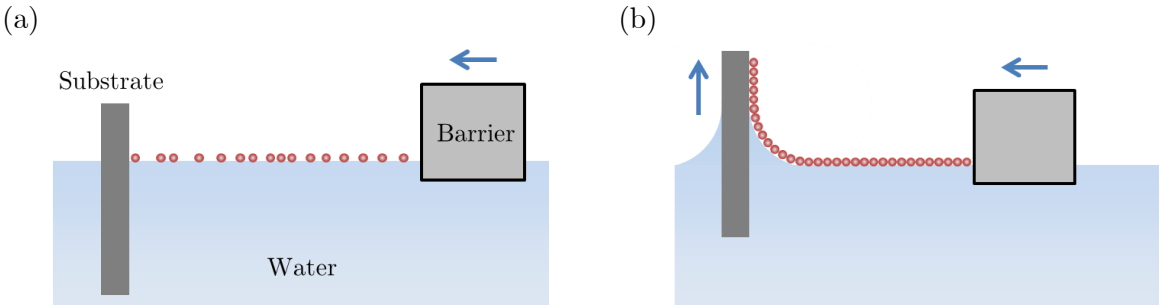

Figure 2.3.1 – Langmuir-Blodgett deposition method.

It also became possible to easily create an organized hexagonal close-packed monolayer of colloids to be used as a precursor mask for posterior material patterning, enabling the fabrication of structures without the use of hard masks and equipment of conventional photolithography, hence lowering production costs. This simple, fast and scalable process consists of the aforementioned steps, which are depicted in Figure 2.3.2.

In the first step, the monolayer of PS microspheres is deposited on different substrate surfaces by applying a Langmuir-Blodgett self-assembly method [33] with a KSV NIMA Langmuir-Blodgett Medium Deposition Trough. Firstly, the trough and barriers are washed – rubbing with detergent and cleaning with water, spraying with IPA and finally filling the trough with deionized water and vacuumed. The system is turned on, two substrates are put, back to back, on the sample holder and the trough is carefully filled with deionized water. Once the surface tension stabilizes, its value is set to 0 and the system calibration is initiated. This stage consists in ensuring the surface tension difference between the system with opened and closed barriers is low (0.3-0.8 mN/m), meaning the water surface has low contaminants. The same process is applied with the substrates dipped. When the calibration is finished, 200 µL of dispersed PS microspheres purchased from *Microparticles GmbH* are diluted in 600 µL ethanol maintaining a 25 µg/mL concentration. With a syringe, the solution is slowly added to the water surface. With the KSV NIMA software, the surface tension threshold value is set to 18 mN/m and the system starts closing the barriers at 10mm/min until said value is met. At this point, the substrate is pulled up at 2mm/min and the deposition begins.

2.3.2 Reactive Ion Etching (RIE)

Depending on various parameters, [34] shown in Table A 1 (Appendix A), the substrate then undergoes a plasma treatment in a reactive ion etching (RIE) system (Trion Minilock Phantom III) where the PS microspheres act as an etching physical mask, resulting in the

Table 2.3.1 – Studied parameters during RIE processing.

Gas	O_2	CF_4	SF_6	O_2/SF_6
Gas Flow (sccm)	10	30	50	100
Power (W)	50	100		
Pressure (mTorr)	45			

formation of dome/pillar-like structures of different size and shape. The processing gas affects the etching rate and surface chemistry as well as selectivity between PS and the substrate. However, for materials with the same polymeric nature as PS does, the selectivity is close to unity (1:1). [35] Importantly, as will be shown in the Results and Discussion section, the progressive lateral etching of the patterned structures (Figure 2.3.2b,c) is an expected effect derived from the etching of the PS spheres. The tested conditions/parameters are presented in Table 2.3.1. The patterned structures were observed resorting to the (Hitachi TM 3030Plus Tabletop) scanning electron microscope (SEM).

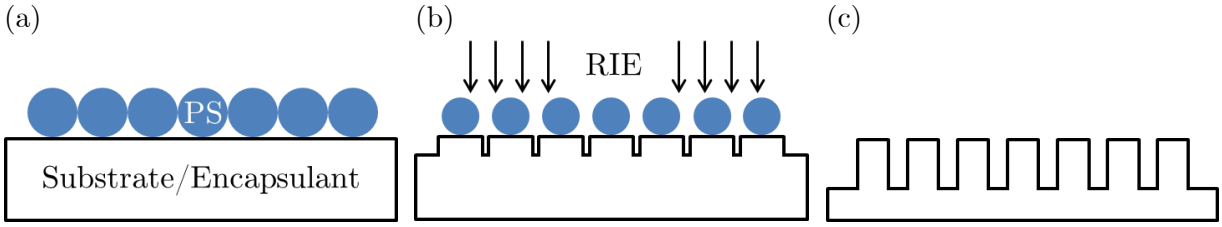

Figure 2.3.2 – Colloidal lithography stages: (a) Deposition of colloidal mask (PS nano/micro-spheres); (b) Substrate patterning by reactive ion etching and consequent mask etching; (c) Surface after sphere removal.

2.4 Contact Angle Measurements

To obtain the static and dynamic water contact angles (CAs) and characterize the surface wettability of glass, PEN, PET and parylene materials, it was used the DataPhysics OCA 15 Plus. The system is composed by a syringe placed vertically and an automatic dispenser. A digital image acquisition system records the droplet's lateral profile. Throughout the study, 2 μL droplets of deionized water were used as reference. The static CA analysis is performed with the embedded software (SCA 20) using the Laplace-Young approximation model with minimum 9 measurements per sample. The dynamic water CAs were measured by dragging the droplet with the needle, as described in section 1.2.

2.5 Optical Characterization

Measurements of transmittance and reflectance of the samples, both in total and diffuse mode were performed using a Perkin Elmer Lambda 950 spectrophotometer equipped with an integrating sphere. The spectra were acquired in the 300-1500 nm wavelength range.

2.6 Surface Characterization

Surface morphology analysis was performed by atomic force microscopy (AFM) (Asylum MFP3D) in tapping mode using an Olympus AC160TS tip (K=26N/m; F_0=300kHz), scanning electron microscopy (SEM) (Zeiss Auriga CrossBeam Workstation) and tabletop

SEM (Hitachi TM 3030Plus Tabletop). Surface chemical composition was acquired via x-ray photoelectron spectroscopy (XPS) (Kratos Axis Supra).

2.7 Solar Cell Fabrication and Opto-electronical Characterization

Two batches of amorphous silicon (a-Si) solar cells, one with p-i-n (superstrate) and the other with n-i-p (substrate) configurations and an active area of 4.91 mm^2 and 20.2 mm^2, respectively, were fabricated by plasma enhanced chemical vapor deposition (PECVD) in the clean room environment of CEMOP – Center of Excellence in Microelectronics Optoelectronics and Processes. The test cells were characterized without any coating, with a flat 5 μm parylene layer and after structuring of the parylene layer, through the measurement of I-V curves and external quantum efficiency (EQE) spectra, which were obtained with an Oriel Instruments Verasol LED solar simulator and a Newport QuantX300, respectively.

3 Results and Discussion

3.1 Screening of base materials

Four materials were chosen to be nano/micro-patterned in this study. They were regular glass, parylene-C, PEN and PET. Glass is the standard material for superstrate use in solar cells due to its excellent transparency, robustness and resistance to environmental degrading agents (such as UV light). PEN and PET are the standard polymeric materials throughout an extremely wide range of applications; they are very transparent, flexible and virtually unbreakable. Parylene has recently been used in microfabrication mainly as encapsulation layer and it presents excellent barrier properties; due to its deposition method, it can form micro- or even nano-layers perfectly conformable to the substrate, pin-hole free. [30]

In this section, the properties of these materials will be compared in order to evaluate their eligibility in this study. Specifically, focusing on transmittance properties, inherent contact angle (CA) and resistance to RIE processing (compatibility with colloidal lithography process).

For that, both total and diffuse transmittances were measured (Figure 3.1.1), as well as the static CAs of regular glass, parylene, PET and PEN. Table 3.1.1 presents the static CAs, and also the average total and diffuse transmittances, which were determined through the integration of the respective curves between 400 and 1400 nm. This interval was considered so the results can be widely used, instead of focusing on a particular solar cell technology (e.g. c-Si, a-Si, GaAs, etc.).

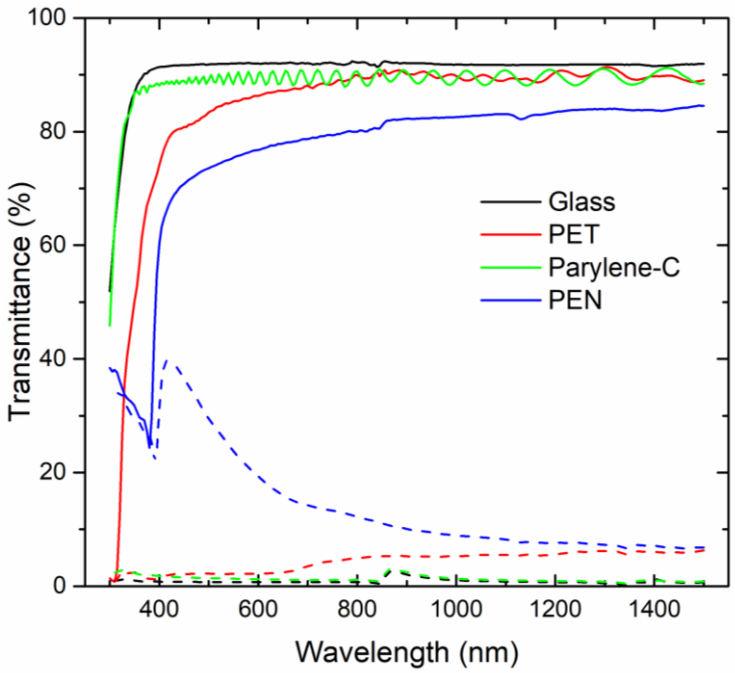

Figure 3.1.1 – Transmittance comparison between different materials. (T_T – solid lines and T_D – dashed lines) It is worth mentioning a step might be observed at 855nm, which is due to the changing of the spectrophotometer I-V lamp to the UV-visible one.

Table 3.1.1 – Contact angles and average transmittance of several untreated surfaces.

	Glass	PET	Parylene	PEN
Avg. T_T (%)	91.8	88,0	89.4	79.9
Avg. T_D(%)	0.9	6.6	1.2	15.9
CA (°)	57.1 ± 1.5	87.4 ± 2.5	98.2 ± 1.3	80.4 ± 1.1

The results show that the CA of glass is extremely low (57°) which is attributed to its high surface energy of ~150mN/m, [12] while PEN's contact angle (CA) is the lowest of the polymers. During the measurements of CA, it was found that PET has very strong adhesion energy to water. When a water droplet was placed on PET it would not "slide", even with the help of the depositing needle. Moreover, PEN has an extremely poor optical performance with an average total transmittance of only 79.9% (while the other materials are close to or above 90%). Although PET has a higher cut-off ultraviolet (UV) wavelength (~500 nm) than parylene and glass (~400 nm), it revealed a very good transmission in the 700-1500nm range.

Also, a dry etching selectivity preliminary test was conducted on glass due to its inherent chemical and physical robustness. Therefore, with the intent of studying the selectivity between glass and PS it was subjected to different plasmas (SF_6, CF_4, O_2, Ar) and plasma combinations (SF_6/Ar, CF_4/Ar, O_2/Ar) with a physical mask of 1.6 μm PS microspheres. It was observed that, after the masking spheres were all etched out, the glass surface had been patterned as presented in Figure 3.1.2, but the aspect ratio of the produced features revealed very low. Thus, despite several RIE intents, it was concluded that glass has an extremely low selectivity to the aforementioned gas-based plasmas, relative to PS microspheres.

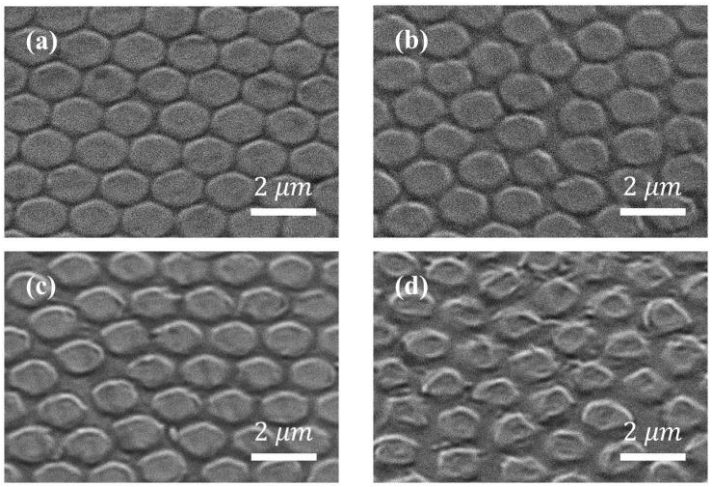

Figure 3.1.2 – RIE of glass, revealing the low selectivity in comparison to the PS mask. (a)5min, (b) 10min, (c) 15min, (d) 20min (100W, SF_6 – 16sccm, Ar – 4sccm, 20mTorr)

The CA of these patterned glass surfaces did not exceed 90° and the selectivity of glass in comparison with PS is very low on the RIE process. Consequently, glass, despite its excellent optical properties, was considered ineligible for this study. The low transmittance of PEN and relatively low CA also made it ineligible. In this work, the studies were, therefore, focused in the optimization of only PET and parylene surfaces for high CA with low hysteresis, as well as strong forward-scattering properties (i.e. high diffuse transmittance).

3.2 Screening of Precursor Microspheres for Patterning

In this section, it is discussed the use of two different sizes of PS colloidal spheres – 1.3 μm and 1.6 μm. They are compared with respect to quality of deposition (self-assembled close-packed monolayer throughout large surface area) and to the wetting and optical properties of the subsequent patterned surfaces with RIE (the last two will be further addressed in section 3.7, therefore, only a comparative analysis will be herein preformed). In Figure 3.2.1 are represented SEM images of both sized microspheres deposited on parylene.

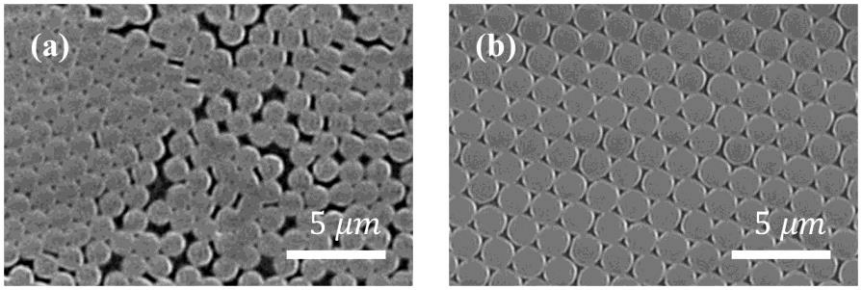

Figure 3.2.1 – SEM images of (a) 1.3 μm PS spheres and (b) 1.6 μm spheres assembly.

The deposited monolayers of 1.3 μm PS spheres (Figure 3.2.1a) were typically characterized by the existence of hexagonal compact zones, although most of the surface is covered with a disordered microspheres monolayer. With 1.6 μm PS spheres the obtained films are very consistent (Figure 3.2.1b). Overall, most depositions present a good hexagonal compact monolayer over large areas (SEM observations revealed extremely ordered areas up to several millimeters) with some sporadic defects (e.g. absence spheres, polycrystalline-like domains). A broader SEM image is available in Figure C 1 (Appendix C). Due to the disorganized characteristic of the particle arrays formed with 1.3 μm PS spheres, the hydrophobicity of parylene surfaces patterned through RIE with these spheres is theoretically lower than that of 1.6 μm sized spheres (Decrease of solid-liquid contact area). However, the comparison shown in Figure 3.2.2 (static CA) suggests that there is little apparent difference. Both surfaces achieved extremely high static CA (161.7° with 1.3 μm and 162,0° with 1.6 μm PS spheres), revealing superhydrophobicity.

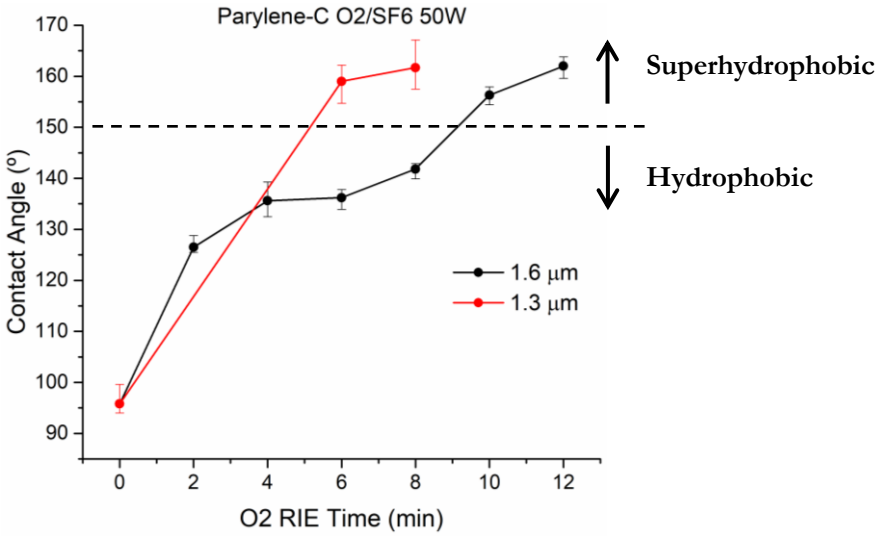

Figure 3.2.2 – Comparison between parylene static contact angles. The dashed line indicates the threshold value for superhydrophobicity (150°)

The influence of PS sphere size on optical performance was herein studied through the comparison of total and diffuse transmittance and reflectance of parylene samples treated with O_2/SF_6 plasma (Figure 3.2.3). The RIE times were fixed at 6 and 8 minutes. Similarly to the procedure in section 3.1, by integrating the obtained spectra it was possible to determine the average values of total and diffuse transmittance, as well as total reflectance, which are presented in Table 3.2.1.

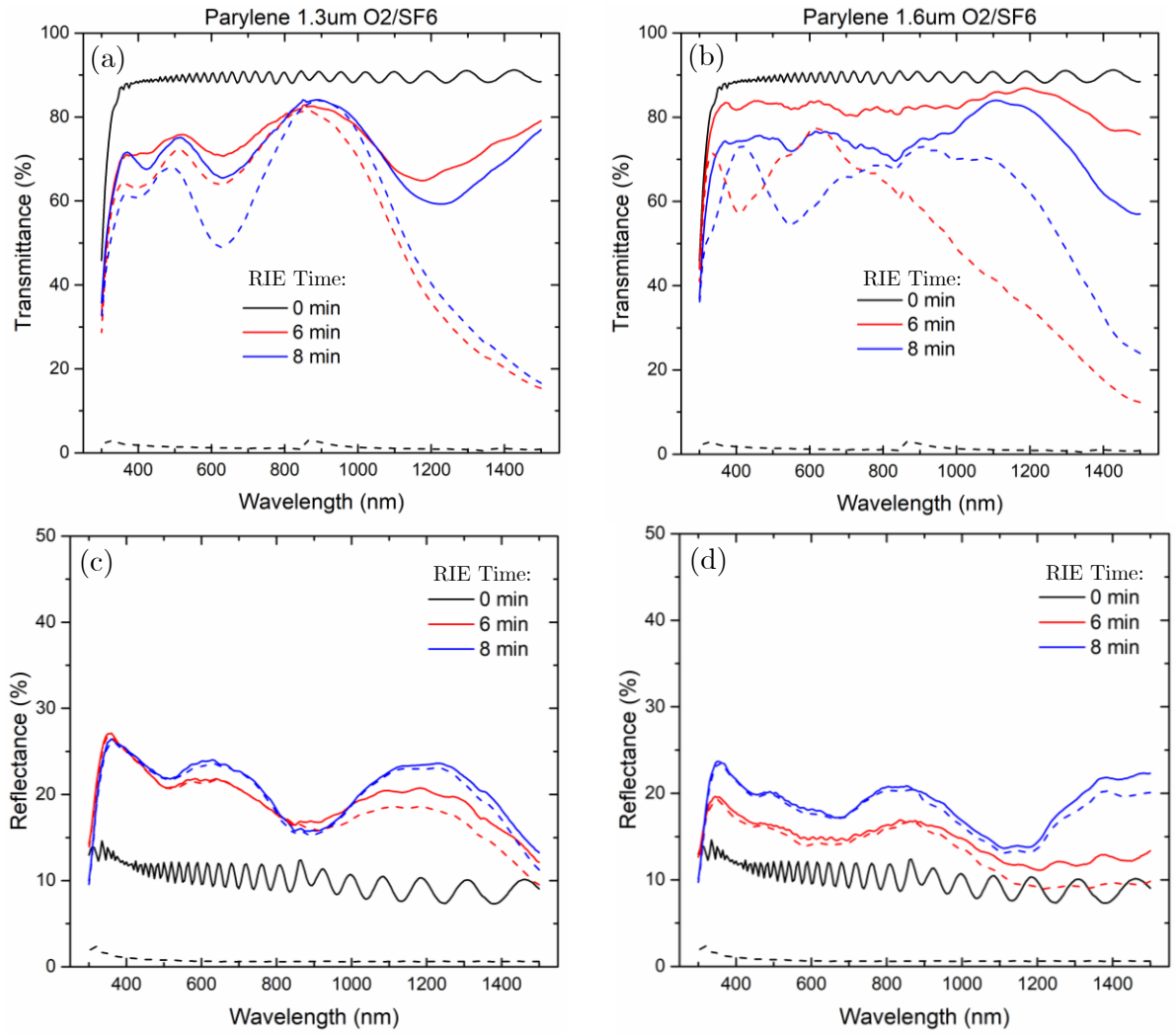

Figure 3.2.3 – Parylene total (solid lines) and diffuse (dashed lines) transmittance/reflectance spectra with different O_2 plasma times using (a), (c) 1.3 μm masking PS spheres and (b), (d) 1.6 μm masking PS spheres.

The peaks in the spectra of the patterned parylene with 6 and 8 minutes of RIE are the consequence of light interference effects caused by the optical behavior of the structures as a 2D honeycomb diffraction grating. Such periodicity effect is more pronounced in the spectra of the surfaces patterned with 1.3 μm PS spheres, since the dimension of these smaller spheres is closer to the observed wavelengths in the NIR. The difference in average transmittance and reflectance values is presented in Table 3.2.1. For the same RIE time, surfaces patterned with 1.3 μm PS spheres have lower T_T and higher R_T than surfaces patterned with 1.6 μm spheres. Due to the higher reliability in the deposition process and the better optical properties of 1.6 μm patterned surfaces, the 1.6 μm PS spheres were considered

the preferential ones for masking purposes in this study, and therefore were the colloids used in the subsequent work.

Table 3.2.1 – Average total and diffuse transmittance and average reflectance of 6 and 8 minute O_2/SF_6 plasma-treated parylene surfaces with 1.3 μm and 1.6 μm masking PS spheres.

		Avg. Total Trans. (%)	Avg. Diff. Trans. (%)	Avg. Total Refl. (%)
6 min	1.3 μm	73.6	59.1	20.9
	1.6 μm	83.0	52.7	15.8
8 min	1.3 μm	70.9	58.2	22.3
	1.6 μm	75.4	62.9	19.5

3.3 Surface Topography Development

3.3.1 Analysis of microspheres' shaping through RIE

Both PET and parylene surfaces were micro-patterned with the CL method of Figure 2.3.2. To study the structuring via RIE, the etching evolution of the spheres was observed and characterized through SEM, as presented in Figure 3.3.1. It is worth mentioning on (a) and (b) the dispersion of PS is due to charging effects in the SEM image acquisition.

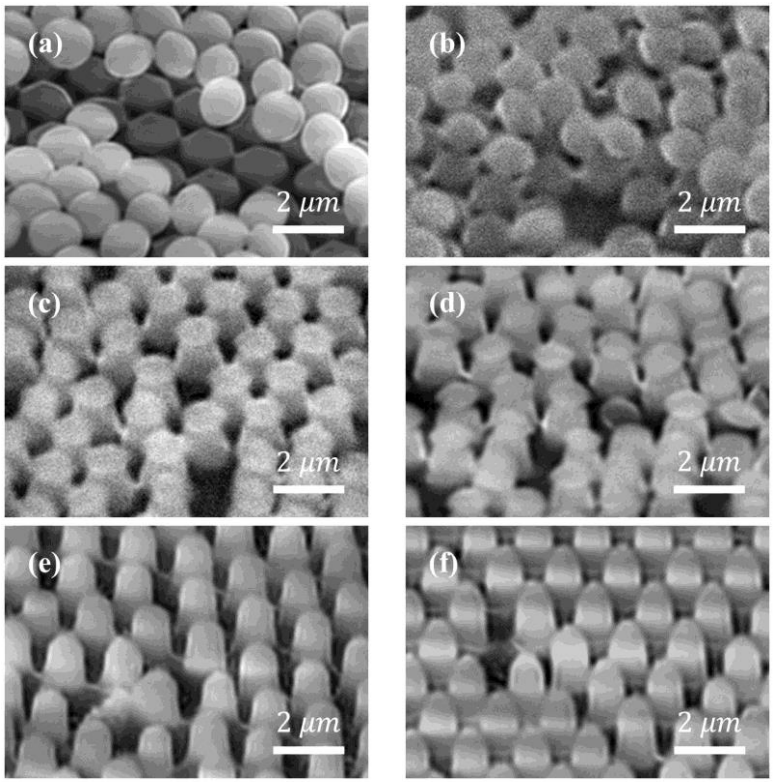

Figure 3.3.1 – (Hitachi Tabletop) SEM images of RIE of PET masked by 1.6 μm PS spheres (a) 20min (b) 30min (c) 40min (d) 50min (e) 60min (f) 70min (50W, SF_6 – 10sccm)

Initially, it is noticeable that, as the process is extremely anisotropic, the PS spheres take an oval shape (etching mainly along the vertical axis, i.e. the plasma incidence direction), practically without decreasing the diameter, allowing the patterned substrate to retain the initial masking diameter (Figure 3.3.1a). Then, after 30 minutes the spheres start thinning (i.e. masked area decreases). From this point on, the spheres' diameter will become progressively smaller, until the process ends. As can be observed, at 70 minutes the spheres

were completely etched. From this process, the PS spheres vertical etching rate was determined as 1.6μm/70minutes resulting in ~23nm/minute. The various PS etching rates are disclosed in Table 3.3.1.

Table 3.3.1 – PS etching rate (approximate values)

SF_6		CF_4		O_2	
50W	100W	50W	100W	50W	100W
$23\ nm/min$	$53\ nm/min$	$41\ nm/min$	$76\ nm/min$	$160\ nm/min$	$266\ nm/min$

3.3.2 Analysis of surface patterning

The contribution of plasma treatment on both PET and parylene surface roughness was studied through SEM and AFM analysis. Top and cross sectional views of the surface with increasing RIE time are presented in Figure 3.3.2 (and Figure C 7).

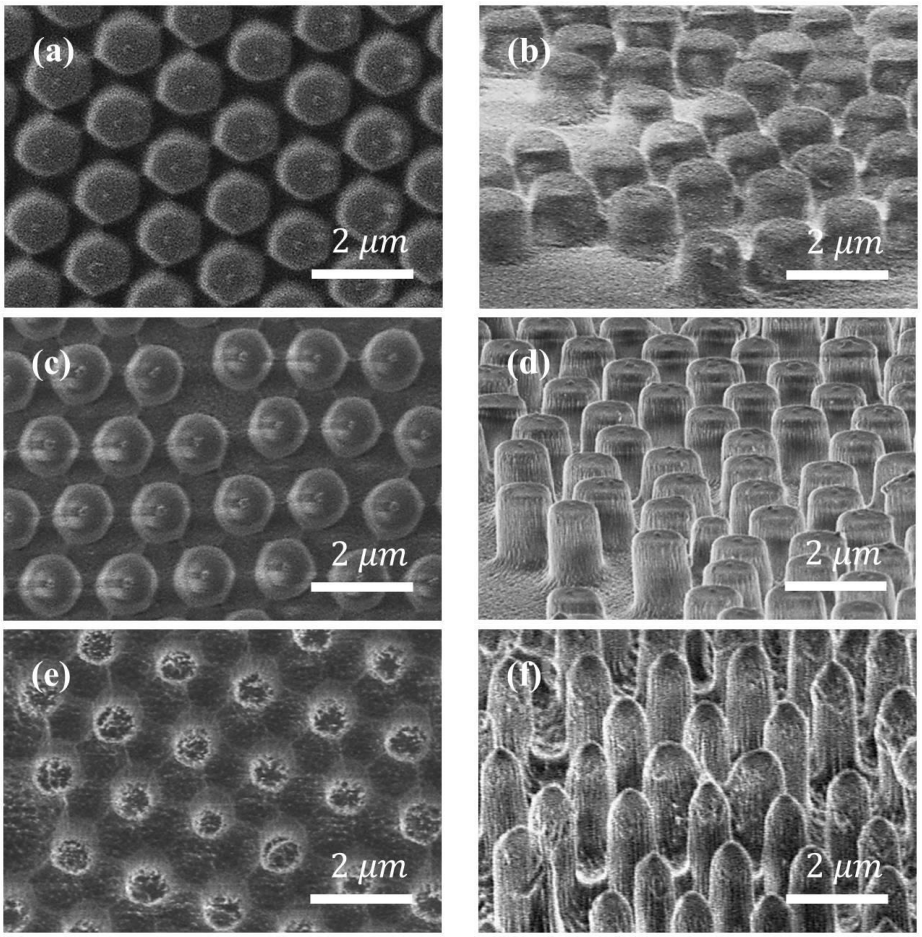

Figure 3.3.2 – Top view (left) and 90° (digitally corrected) cross sectional view (right) SEM images of etched PET (a), (b) 30min (c), (d) 50min (e), (f) 70min (50W, SF_6 – 50sccm)

The surface etching initiates with the preservation of the original diameter of the masking PS spheres, resulting in the formation of cylinders in the material underneath the spheres (Figure 3.3.2b). Then, as the spheres' diameter starts decreasing, the cylinders' diameter follows that decrease, due to the extremely high anisotropy (directionality) of this treatment (Figure 3.3.2d). When the masking spheres reach a certain (low) diameter, it starts decreasing rapidly. Here the cylinders' top acquires a dome-like shape as presented in Figure

3.3.2f. Also, the formation of nano-roughness in the spaces between the cylinders was observed and analyzed in section 3.3.3. The cross sectional images were obtained by digitally adding a 20° correction factor to a 70° image in order to correctly measure the dimensions of the observed structures. These dimensions and the approximate etching rate are specified in Table 3.3.2. The patterned structures on parylene presented a slightly lower aspect ratio due to the, also slightly lower selectivity, relative to PS spheres.

Table 3.3.2 - Average diameter and height, with corresponding standard deviation, of the surfaces presented in Figure 3.3.2, as well as estimated etch rate by SEM.

	30min	**50min**	**70min**
Average Diameter (µm)	1.28 ± 0.05	1.14 ± 0.04	0.92 ± 0.06
Average Height (µm)	0.92 ± 0.06	1.46 ± 0.07	2.15 ± 0.14
Etch Rate (nm/min)		~30.2	

AFM 3D images and cross sectional profiles were acquired in order to compare with SEM results (Figure 3.3.3 and Figure C 2). It is worth noting that, because of the high aspect ratio of the surface structures, the AFM tip could not sense the base of the sample, which introduces a measurement error. As observed in, both SEM and AFM data, the produced structures are extremely rough which can be beneficial for hydrophobicity purposes, yet can be disadvantageous on the surfaces' optical properties, which will be discussed in section 3.7.

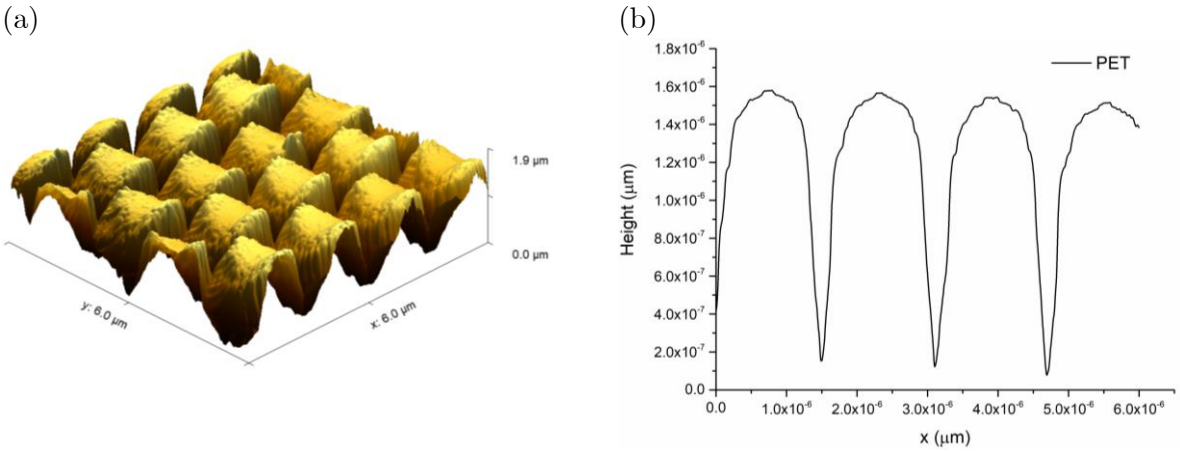

Figure 3.3.3 – (a) AFM 3D image of 70min etched PET with 1.6 µm PS spheres (50W, SF_6 – 50sccm) and (b) respective AFM cross section profile.

In Table 3.3.3 are the average diameter and average height of the above surface. It is clear that, comparing with the results obtained through SEM analysis (Table 3.3.2), the measurements have a positive error in diameter due to geometrical convolution effects, and a negative error in height because the tip could not reach the base of the sample.

Table 3.3.3 – Average diameter and height and respective standard deviation of the surface presented in Figure 3.3.3 by AFM.

	70min
Average Diameter (µm)	1.30 ± 0.04
Average Height (µm)	1.55 ± 0.03

3.3.3 Analysis of RIE-induced nano-roughness

As mentioned in the previous section, a nano-roughness has been patterned in the regions between the etched pillars, resulting from the direct exposure of the surface to the incident plasma. To study the effect of such nano-roughness alone (i.e. without the micro-pillars), the analysis of control samples was performed, which underwent RIE without the use of CL, in order to more accurately characterize the surface's topology and also to evaluate the wettability of the RIE-induced nano-roughness reported earlier in section 3.3.2. The entire process was repeated without masking spheres and observed through SEM and AFM. The acquired images are presented in Figure 3.3.4.

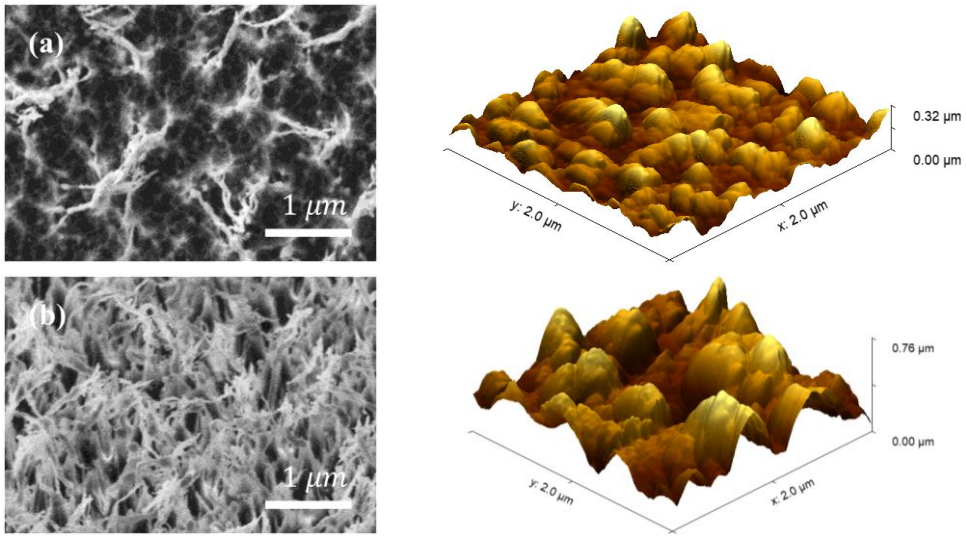

Figure 3.3.4 – Parylene O_2/SF_6 treated surfaces without masking PS spheres. (a) 4 min (b) 10 min.

The plasma treatment generated "nano hair" which was poorly detected through AFM technique due to the extremely disordered and rough character of the samples. Nonetheless, with increasing RIE time, it was observed an increase in length and density of nano hair. With 4 minutes of O_2/SF_6 plasma the maximum nano hair length was 0.32 μm. When treated for 10 minutes, the maximum height increased to 0.76 μm. It is worth noting that these surfaces also presented superhydrophobicity. However, they have a rather strong pinning effect (droplet movement prevented by local defect that pins the droplet), possibly due to the randomness of the plasma process which would allow the occurrence of localized water impregnation.

3.4 Surface Chemistry Analysis

Wettability modification is not only a consequence of nano/micro-structuring, as provided by the structures fabricated via the previously described methods, but can also be strongly affected by surface chemical modification by the introduction of functional groups.

The analysis of surface chemistry was performed through x-ray photoelectron spectroscopy (XPS). The study was applied to three samples of parylene. The first was untreated, the second was submitted to 5 minutes of O_2-based plasma treatment and the third was also treated with 5 minutes of O_2-based plasma treatment and an additional minute of SF_6-based plasma treatment. None of the samples had PS spheres as mask (as those in subsection 3.3.3). This experiment was conducted in order to justify the abrupt alterations of wettability that go beyond the effect of surface roughness, as proved in section 3.4.

The survey spectra and corresponding fitted high-resolution carbon 1s (C1s) spectra of parylene surfaces are presented in Figure 3.4.1. Compared to the untreated parylene surface, a significant increase in oxygen was observed on the O_2 plasma-treated sample and, with less intensity, on the O_2/SF_6 plasma-treated surface. Moreover, it was detected a heavy increase in the fluorine atomic concentration on the O_2/SF_6 plasma-treated surface. On the O_2 plasma-treated sample, a small amount of fluorine was detected, which can be attributed to a contamination in the RIE chamber. These modifications suggest that new functional groups were formed through the reaction between plasma-surface. The quantification of surface atomic concentration of the untreated, O_2 plasma-treated and O_2/SF_6 plasma-treated samples is presented in Table 3.4.1.

Table 3.4.1 – Quantification of surface atomic concentration

	Untreated	**O_2 Plasma**	**O_2/SF_6 Plasma**
O 1s	1.70	28.26	5.23
F 1s	0.11	5.26	43.17
Cl 1s	8.40	3.42	3.30
C 1s	89.80	63.05	48.30

The presence of O and F on the untreated parylene is attributed to contamination from air (transportation from clean room to XPS) and gloves, respectively. On the O_2 plasma-treated sample, as expected, oxygen functional groups were introduced to the surface [24] and a contamination of F was detected, which can be related to contamination from RIE chamber. On the O_2/SF_6 plasma-treated parylene surface it is observed the almost complete substitution of oxygen by fluorine functional groups. [24] The deconvoluted peaks' binding energies and full width at half maximum (FWHM) are presented in Table C 1. The deconvoluted C1s spectrum of the untreated parylene verified the presence of C-C and C-Cl at 284.8 eV and 285.9 eV, respectively. With that as a reference, the C1s spectrum of the O_2-treated parylene indicated the formation of new peaks at 286.9 eV (C=O), 287.9 eV (O-C=O), 289.2 eV (CF), 290.1 eV (CF_2) and 291.5 (CO3). [22], [24] It is worth noting that the presence of fluorinated groups was very weak. The C1s spectrum of the O_2/SF_6 plasma-treated parylene revealed the presence of CF and CF_2 previously detected peaks, though with much more intensity, and detected a new peak at 293.7 eV (CF_3). [22], [24]

(a)

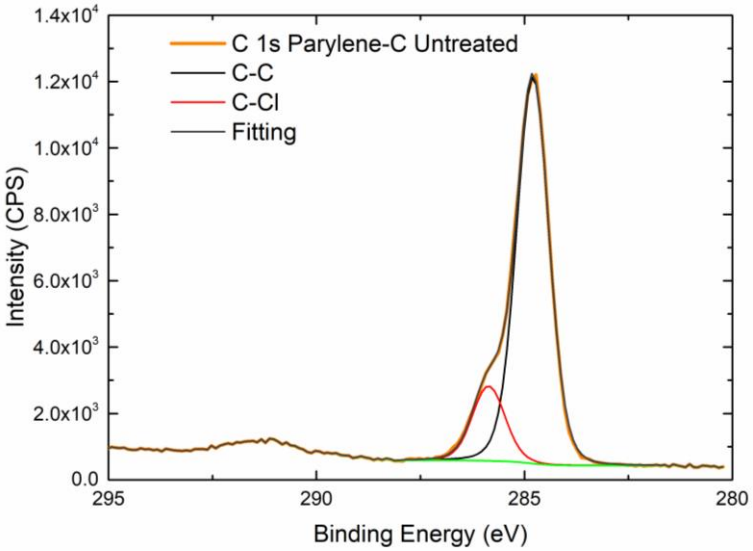

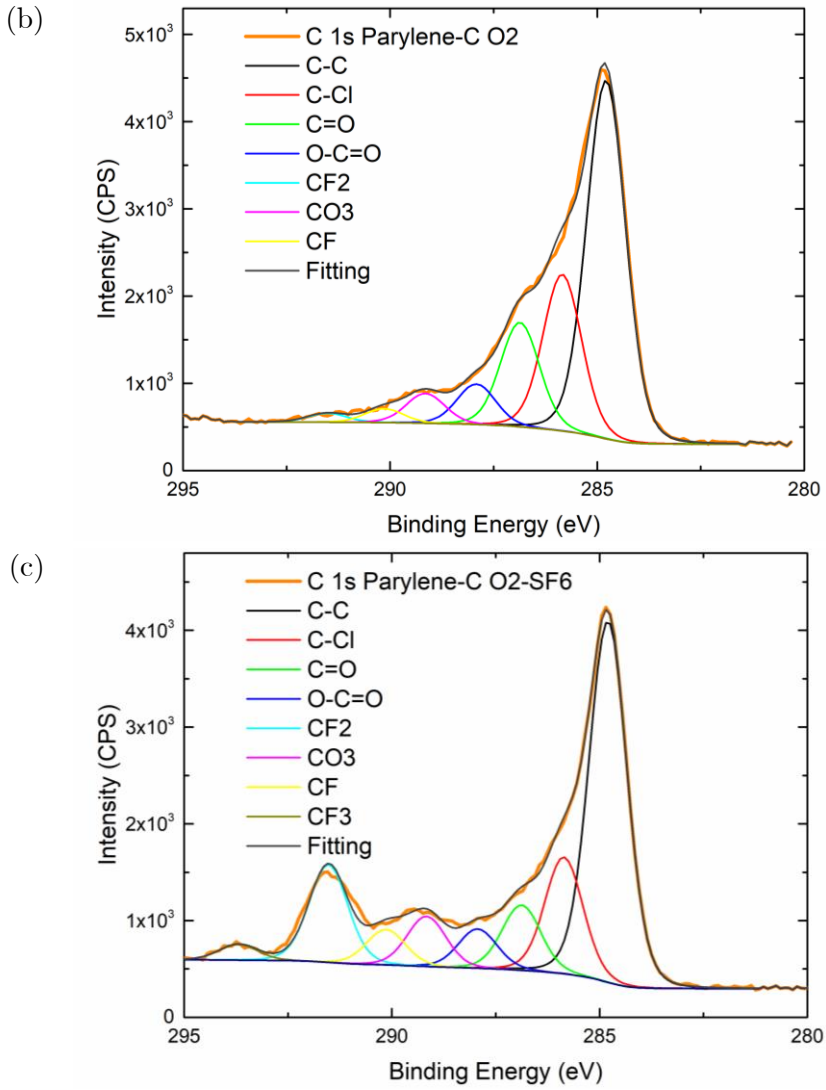

Figure 3.4.1 – X-ray photoelectron spectroscopy spectra of (a) untreated parylene, (b) 5min O_2 plasma-treated parylene and (c) 5min O_2 and 1min SF_6 plasma treatment.

The chemical inertness of the fluorinated groups, therefore, contributes to the lowering of the surface energy, which in turn enhances the surface's hydrophobicity. The O_2 plasma pre-treatment provided the reactivation of the inert parylene surface, enabling the subsequent substitution of oxygen by SF_6. [22], [24] The results presented in this section will have a rather significant role in the wetting properties analyzed in section 3.5.

3.5 Contact Angle Measurements

3.5.1 Static Water CA

To understand the influence of the etching gas, radio frequency (RF) power and gas flow during RIE on CA, each parameter was varied, maintaining a constant pressure. This thorough analysis was performed on PET, in order to obtain the preferential RIE treatment conditions to maximize the CA. Then, this optimized RIE treatment was applied in parylene. Also, following up on previous work, [22] a 2-step RIE treatment was tested as described below. The obtained static CAs for PET surfaces masked with 1.6 μm PS spheres are presented in Figure 3.5.1.

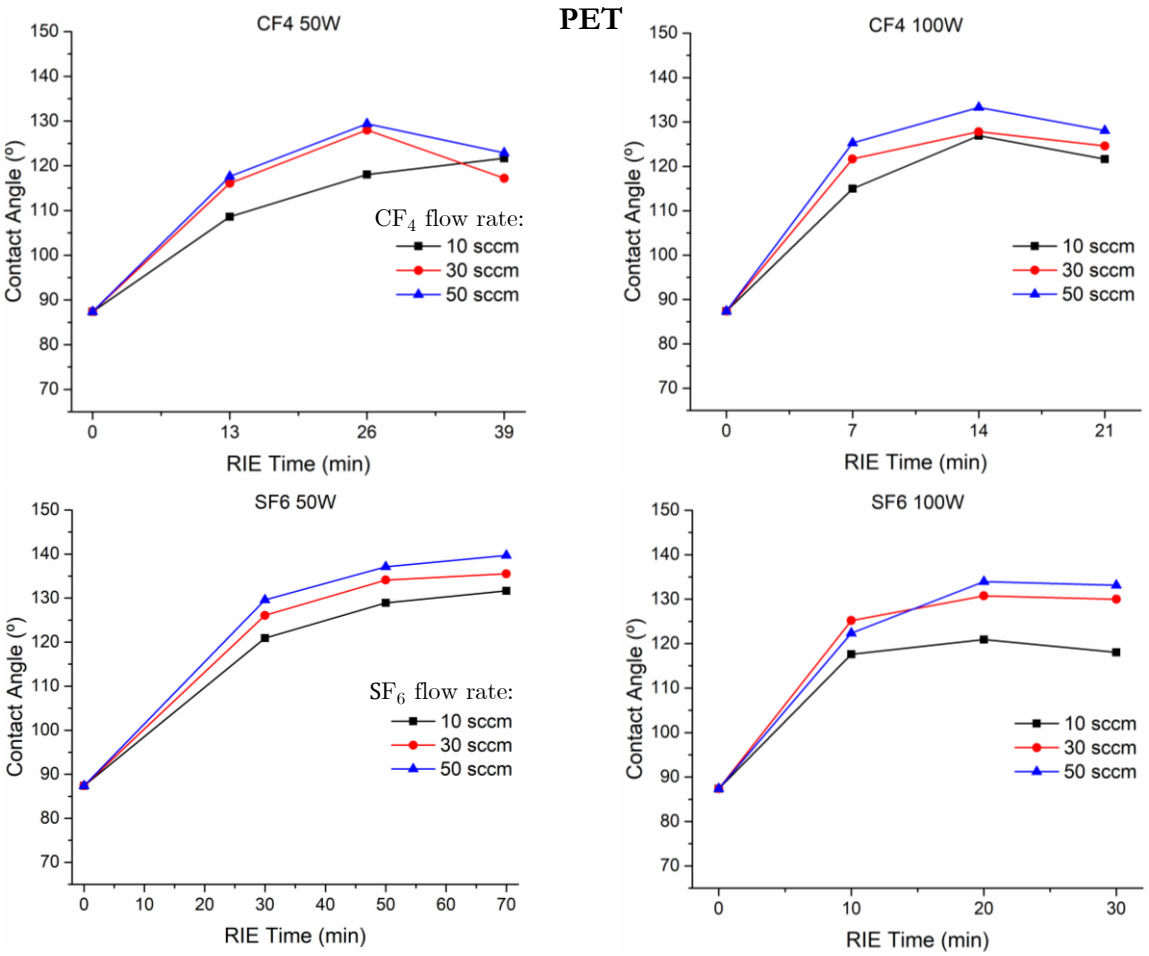

Figure 3.5.1 – Static CA of PET surfaces treated with different plasmas, RF power and RIE time with 1.6 μm PS spheres.

There are two parameters influencing PET's surface hydrophobicity. The first is surface roughness. It is clear that (as addressed in section 3.3) increasing the RIE time results in the increasing of the micro pillars height, which in turn has an effect on the measured CA. The second parameter is the surface chemistry modification (observed via XPS for parylene in section 3.4). The analysis of Figure 3.5.1 suggests that SF_6-based plasma produces a slightly more hydrophobic effect than CF_4-based plasma, which is also reported on [24]. It is observed that higher gas flow enables higher hydrophobicity. This fact may be due to the higher concentration of fluorinated groups interacting with PET's surface. The increase of RF power, from 50W to 100W, with SF_6 plasma caused a decrease of CA. This could be related to surface geometric properties (higher anisotropy), rather than chemistry properties. However, with CF_4 plasma the influence of higher RF power appears to be minor.

Surfaces treated with O_2-based plasma revealed extremely high hydrophilicity, causing the complete surface wetting, precluding the CA measurement. A previous study [22] introduced a 2-step plasma treatment comprehending the application of RIE with O_2 followed by RIE with SF_6, called "consecutive-O_2-SF_6" (COS) plasma treatment. In this study, the O_2-based RIE time was varied from 20s to 10 min. Then, 1 min of SF_6-based RIE would be performed. A maximum CA of ~169° was reported. It is, therefore, herein applied the same treatment sequence, with slight variation of RIE parameters. The measured CAs of parylene with increasing O_2 plasma time and the CAs of the optimized SF_6-based RIE treatment are presented in Figure 3.5.2.

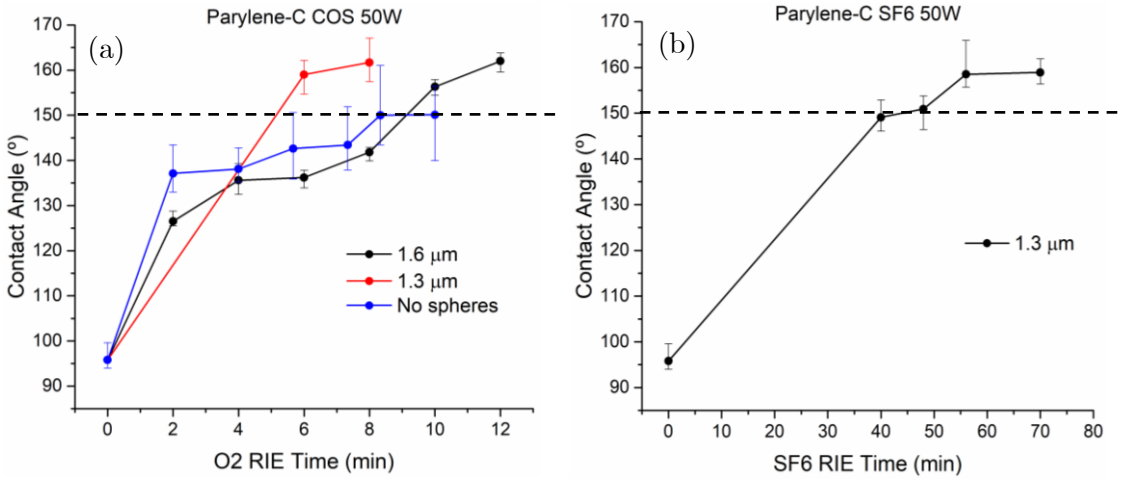

Figure 3.5.2 – CA obtained through (a) COS treatment without spheres and with different sphere sizes and (b) SF_6-based treatement. The dashed line indicates the superhydrophobic threshold of 150°.

The CA registered through the optimized SF_6 plasma treatment of parylene (158.9°) is much higher than that of PET (139.7°). With the COS treatment, it was possible to reduce the etching time to 8 and 12 minutes for surfaces patterned with 1.3 µm and 1.6 µm PS sphere masks, respectively, obtaining CAs of 161.7° and 162.0°. The "maskless" samples presented high CA, however as depicted by the error bars, this treatment provided low homogeneity throughout the surface. Moreover, a pronounced pinning effect was observed, as stated in section 3.3.

Though static CA provides a general idea of surfaces' wettability, as previously discussed in section 1.2, it is not reliable for accurate characterization of non-ideal surfaces' wetting properties. To correctly and more precisely determine whether a surface is hydrophobic, superhydrophobic or adhesive, dynamic CA measurements have to be performed. The dynamic CA of O_2/SF_6 plasma-treated parylene surface is presented in Figure 3.5.3.

3.5.2 Dynamic Water CA

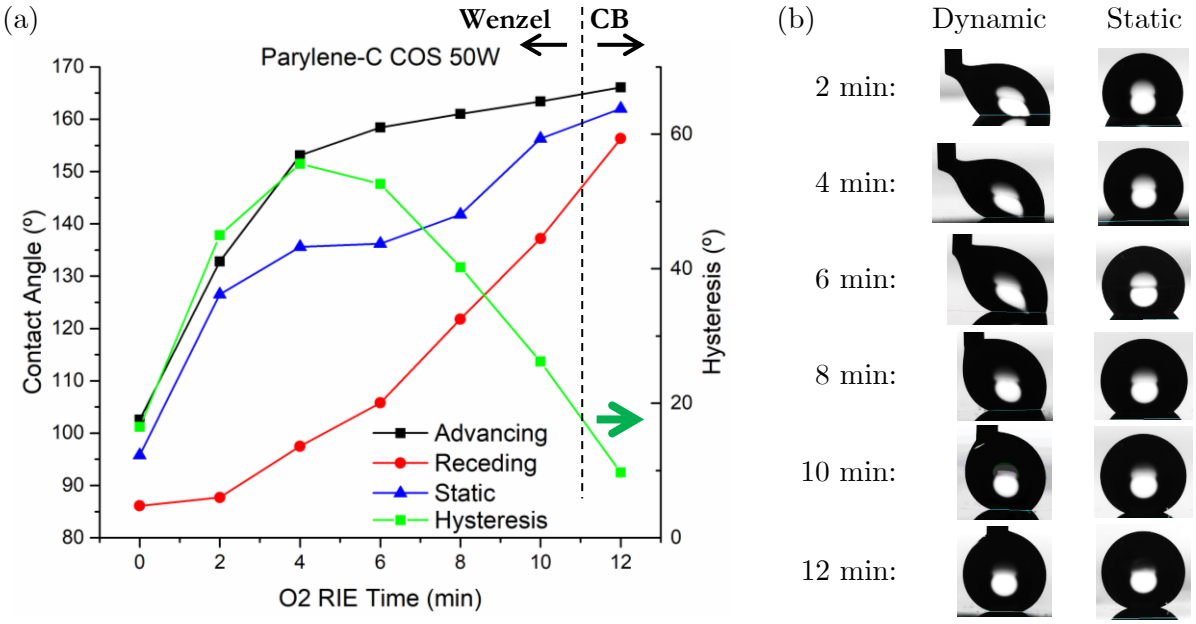

Figure 3.5.3 – (a) Static and dynamic contact angles of Parylene with different O_2 plasma treatment times and 1min SF_6 using a 1.6 µm PS sphere mask and (b) respective droplets' profiles.

Figure 3.5.3a presents information, not only regarding the surface CA, but also correlates with the roll-off angle, thus the surface adhesion. The analysis of CA hysteresis ($Hys = ACA - RCA$) suggests the existence of four states, depending on surface roughness. The first state is characterized by the untreated surface's smoothness and homogeneity. This state comprehends low CA ($\pm$ 95°) and low hysteresis (16.5°). The second is the Wenzel state (2 to 8 min RIE), presenting very high hysteresis (~50°) that is related to a highly adhesive behavior, explained by the occurrence of total impregnation. The third state is the transition between Wenzel and Cassie-Baxter states. Although it cannot be effectively specified, the partial impregnation is present between 10-12 min of RIE, which reveals very high CA (>150°) with decreasing hysteresis. Finally, the last state is the Cassie-Baxter state which comprises the highest CA and extremely low hysteresis (~10°). In Figure 3.5.3b, it is possible to observe the different shapes assumed by water droplets, to minimize the surface energy. Figure C 3 presents the dynamic CA with only SF_6 RIE. PET samples presented extremely high adhesion; therefore, dynamic CA measurements were not possible to perform because the water droplet would not "slide" through the surface. Moreover, the "maskless" parylene samples with RIE-induced nano-roughness (section 3.3.3) revealed highly disperse dynamic CA measurements (on the same surface, hysteresis ranging from <10° and >30°) due to the previously mentioned pinning effect and low homogeneity of the surfaces. Therefore, dynamic CA measurements were only performed on surfaces with patterned structures (with CL), reaching the Cassie-Baxter state with CA hysteresis as low as 10°.

Even though parylene "maskless" samples provide a superhydrophobic static CA (~150°), they cannot provide the water roll-off effect needed for self-cleaning applications. However, parylene surfaces patterned with CL have extremely high static CA (~162°), while presenting very low CA hysteresis (10°), thus providing the roll-off effect.

3.6 Analytical Comparison of Wettability Properties

In this section the experimental results are compared with the Wenzel and Cassie-Baxter models (section 1.2). It is expected that, due to the chemical alterations applied to the tested surfaces, some discordance between the presented models and the modified surfaces should arise. Recollecting equations 1.2 and 1.3 describing Wenzel and Cassie-Baxter models,

$$\text{Wenzel:} \qquad cos\theta^* = R_f cos\theta_0 \tag{3.1}$$

$$\text{Cassie-Baxter:} \quad cos\theta^* = R_f f_{SL} cos\theta_0 - 1 + f_{SL} \tag{3.2}$$

where $R_f > 1$ and $0 < f_{SL} < 1$ are the ratio of actual solid surface area to its flat projected area and fraction of solid-liquid contact interface, respectively. To calculate R_f, SEM images are used in order to obtain the following geometrical parameters:

- Average Height, h_{avg}
- Average Diameter, d_{avg}

In order to simplify the calculations, the structures are assumed to be in a perfect hexagonal close-packed organization and the simulated area is determined as suggested by Figure 3.6.1. The flat projected area is defined so the number of structures is an integer. Next, the required parameters for comparison with the theoretical models will be determined.

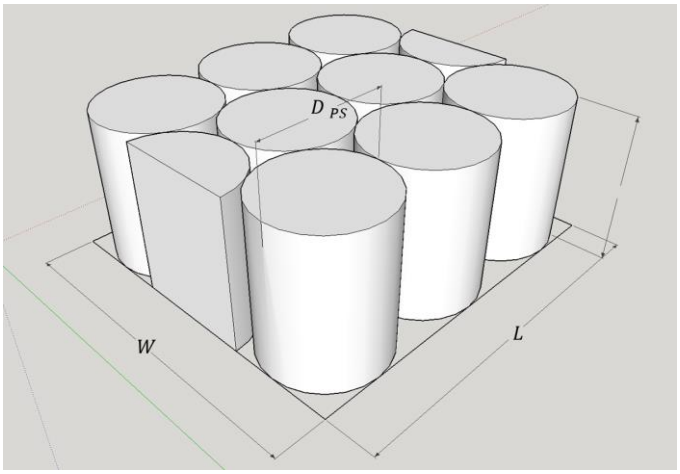

Figure 3.6.1 – Graphical representation of parameters to be included in the models. In this example, $n_1 = 3$ *and* $n_2 = 3$.

If n_1 is the number of cylinders in a horizontal row and n_2 the number of rows, the total number of cylinders is given by

$$n_{Total} = n_1 \times n_2 \tag{3.3}$$

Then, if D_{PS} is the diameter of the masking PS sphere, the length, L, is thus obtained by

$$L = D_{PS} \times n_1 \tag{3.4}$$

The width, W, is given by

$$W = D_{PS}[1 + \cos(30)(n_2 - 1)] \tag{3.5}$$

Finally, the flat projected area, A_{flat}, is given by

$$A_{flat} = L \times W = D_{PS}n_1 \times D_{PS}[1 + \cos(30)(n_2 - 1)] \tag{3.6}$$

From d_{avg}, it's possible to obtain the perimeter, p_{avg}, the area, a_{avg}, of the circular top. Then, with h_{avg}, the single cylinder's area, a_{cyl}, is obtained

$$a_{avg} = \pi\left(\frac{d_{avg}}{2}\right)^2 \tag{3.7}$$

$$p_{avg} = d_{avg}\pi \tag{3.8}$$

$$a_{cyl} = a_{avg} + p_{avg} \times h_{avg} \tag{3.9}$$

At this point, the fraction of solid-liquid contact interface, f_{SL}, is given by the ratio between the area of all the cylinders' top, $a_{SL} = n_{total}a_{avg}$, to the flat projected area, A_{flat}.

$$f_{SL} = \frac{a_{SL}}{A_{flat}} \tag{3.10}$$

Then a_{cyl} is multiplied by the total number of cylinders, n_{Total}, resulting in the total cylinder area,a_{n_cyl}. The real surface area, A_{real}, is obtained by adding the flat projected area, A_{flat}, excluding the cylinders' top surface $n_{total}a_{avg}$ as follows:

$$A_{real} = a_{n\_cyl} + \left(A_{flat} - a_{SL}\right) \tag{3.11}$$

Moreover, R_f is given by

$$R_f = \frac{A_{real}}{A_{flat}} = \frac{a_{n\_cyl} + \left(A_{flat} - n_{total}a_{avg}\right)}{D_{PS}n_1 \times [D_{PS} + x(n_1 - 1)]} \tag{3.12}$$

The Wenzel, Cassie-Baxter and experimental CAs are presented in Table 3.6.1.

Table 3.6.1 – Comparison between CA values calculated through both Wenzel and Cassie-Baxter models and experimental values.

	PET 1.6 μm SF_6 50W 50sccm			Parylene 1.3 μm SF_6 50W 50sccm		
Time (min)	30	50	70	40	56	70
Wenzel	82.9	80.9	80.1	103.9	107.5	108.5
Cassie-Baxter	103.9	114.2	130.4	126.4	134.2	140.5
Experimental	129.6	137.1	139.7	149.1	158.5	158.9

As presented in Table 3.6.1, the Wenzel model predicts that an inherently hydrophilic surface becomes more hydrophilic when the surface roughness is increased and if the surface is inherently hydrophobic it becomes more hydrophobic. The parameters for the calculation of CA through both Wenzel and Cassie-Baxter models are presented in Table C 2.

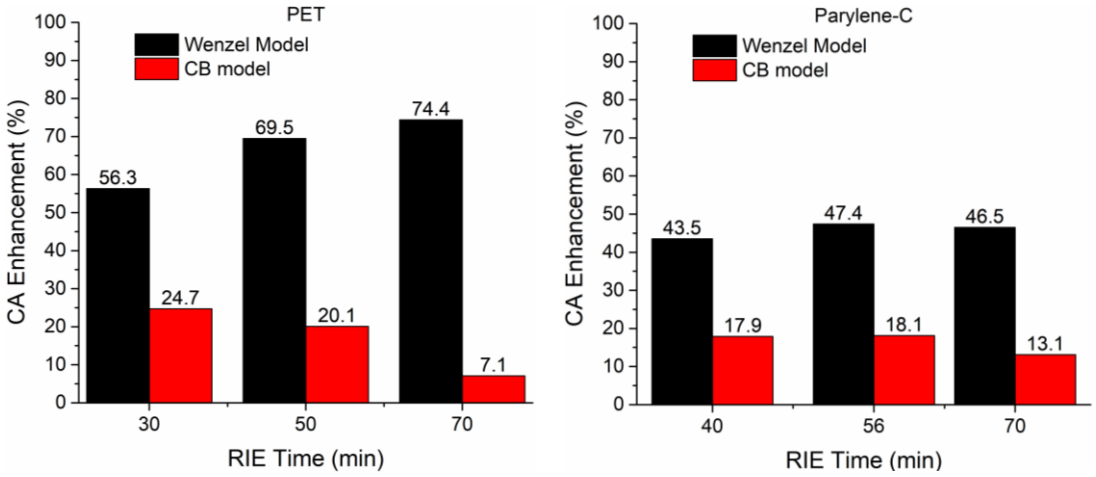

Figure 3.6.2 – Contact angle gain (%) due to surface chemistry modification with different RIE time.

In contrast with Wenzel model, Cassie-Baxter's CA increases with increasing roughness, whether the surface is hydrophilic or hydrophobic. The experimental results surpass both models. This is related to the surface chemistry modification introduced by plasma treatment, as suggested by the results of section 3.4. The CA enhancement induced by chemistry modification, relative to the CA predicted by the aforementioned theoretical models is shown in Figure 3.6.2.

The difference between Wenzel CA and experimental results is significantly higher than that between Cassie-Baxter CA and experimental results, especially for PET surfaces. While Wenzel CA is predicted to decrease, the measured CA increases with RIE time. It is also observed that, whereas for PET surfaces Wenzel and Cassie-Baxter models' have, respectively, a divergent and a convergent behavior in relation to experimental results, for parylene surfaces the gain is roughly constant with RIE time.

3.7 Optical Measurements

The effect of the application of plasma treatments on the optical properties of PET (masked with 1.6 PS spheres) and parylene (masked with 1.3 PS spheres) were herein investigated. The use of SF_6 plasma or the sequential O_2/SF_6 plasma treatments presented similar results, only differing on treatment time. In this section, PET and parylene surfaces with the same SF_6 plasma treatment will, therefore, be studied as they possess different optical and wetting properties. It is crucial in solar cell coating design that the transmittance

losses are kept to a minimum. It is also very beneficial to the solar cell performance to boost the diffuse transmittance, which results in improved light scattering and, thus, increased optical path length. This effect is especially important to increase the absorption of the longer wavelengths in thin-film solar cells. Total and diffuse transmittances of PET and parylene surfaces are presented in Figure 3.7.1.

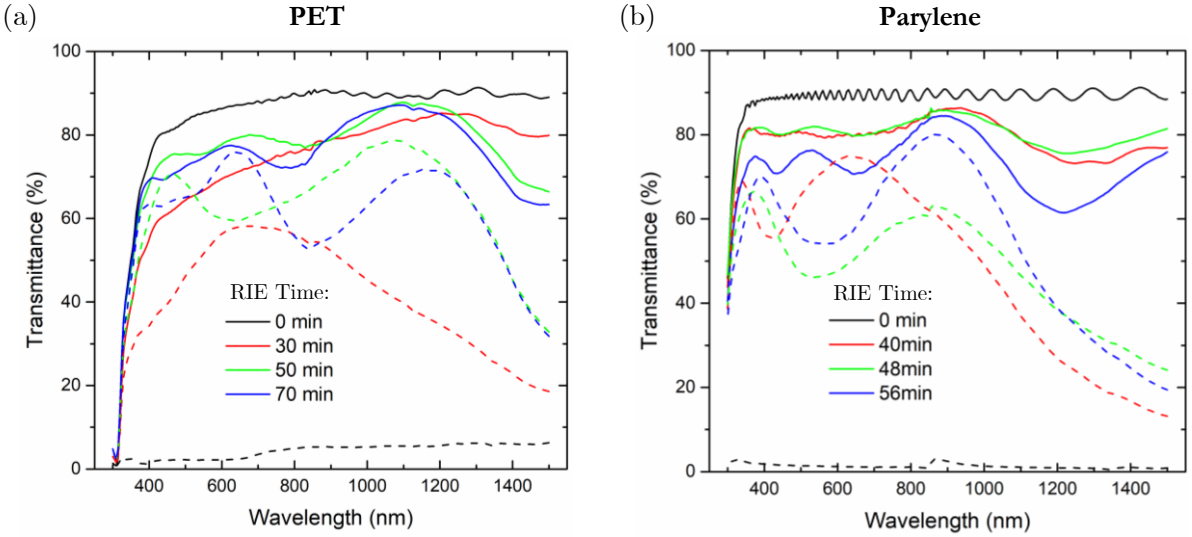

Figure 3.7.1 – Total (solid lines) and diffuse (dashed lines) transmittance of (a) PET and (b) parylene. (SF_6 50sccm, 50W)

There is a slight decrease in total transmittance and an increase in reflectance (Figure 3.7.2), which is related to the nature of the RIE processing. The introduction of periodic structures with a non-smooth character also contributed to that effect. Also, with increasing RIE time it was observed the samples were suffering a whitening effect. This effect is thought to be the consequence of the rough character of the plasma-treated surfaces. It is also possible (though unlikely) that during plasma treatment re-deposition of polymeric material occurs, since Ar is not used. Furthermore, this increasing in reflectance was only observed when parylene was deposited on glass. As will be discussed in section 3.8, this parylene coating actually lowers the reflectance when deposited onto an absorber medium like that of a solar cell.

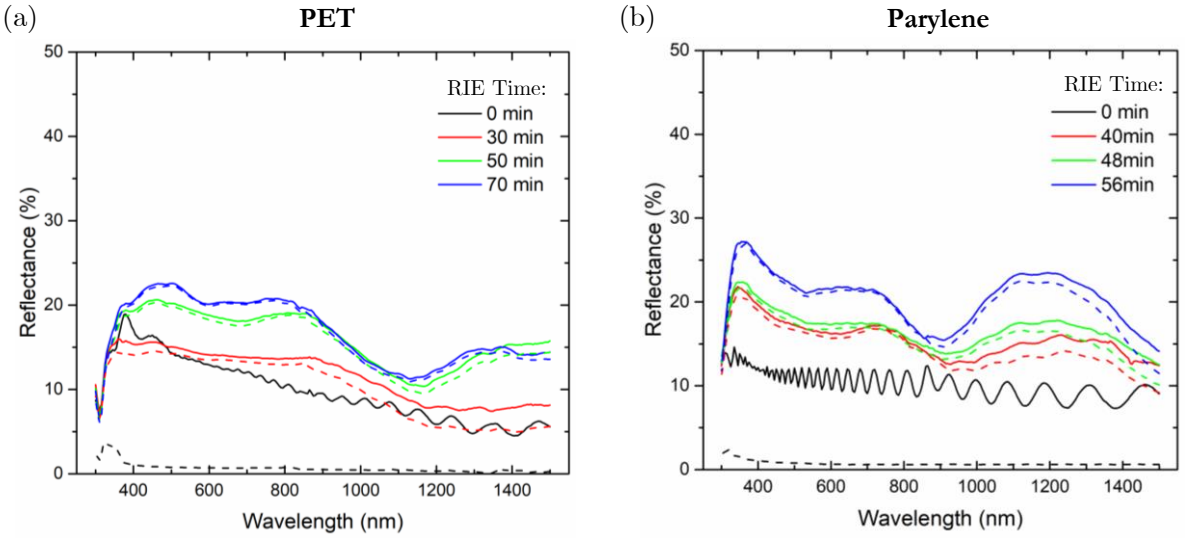

Figure 3.7.2 – Total (solid lines) and diffuse (dashed lines) reflectance of (a) PET and (b) parylene with varying SF_6 plasma treatment time. (SF_6 50sccm, 50W)

In Figure C 4 an interesting results is presented – On a SF_6 plasma-treated PET surface, its transmittance exceeded that of untreated PET at ~1100 nm (The remaining RIE conditions are presented in Appendix C).

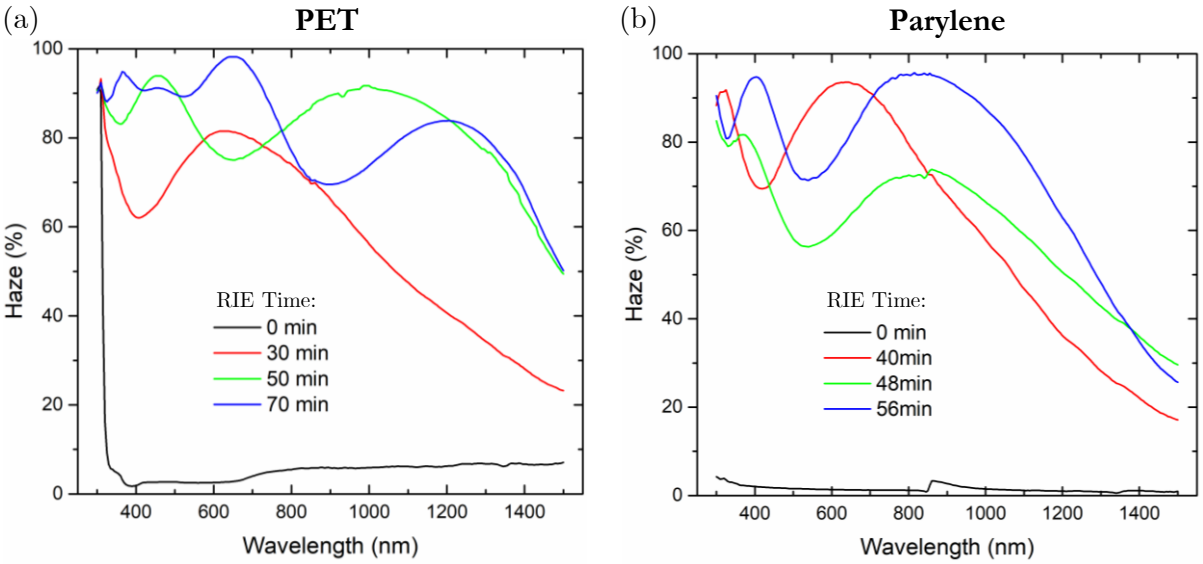

Figure 3.7.3 – Haze in transmittance (equation 1.4) spectra of (a) PET and (b) parylene surfaces with varying SF_6 plasma treatment time. (SF_6 50sccm, 50W)

As presented in Figure 3.7.3, the haze caused by the induced roughness is almost 100% in certain wavelength. This is highly promising for solar cell applications, especially because this scattering effect is extended throughout the entire spectrum of interest and it is extremely intense in the NIR region. In Figure 3.7.4 are presented the absorbance spectra of PET and parylene samples.

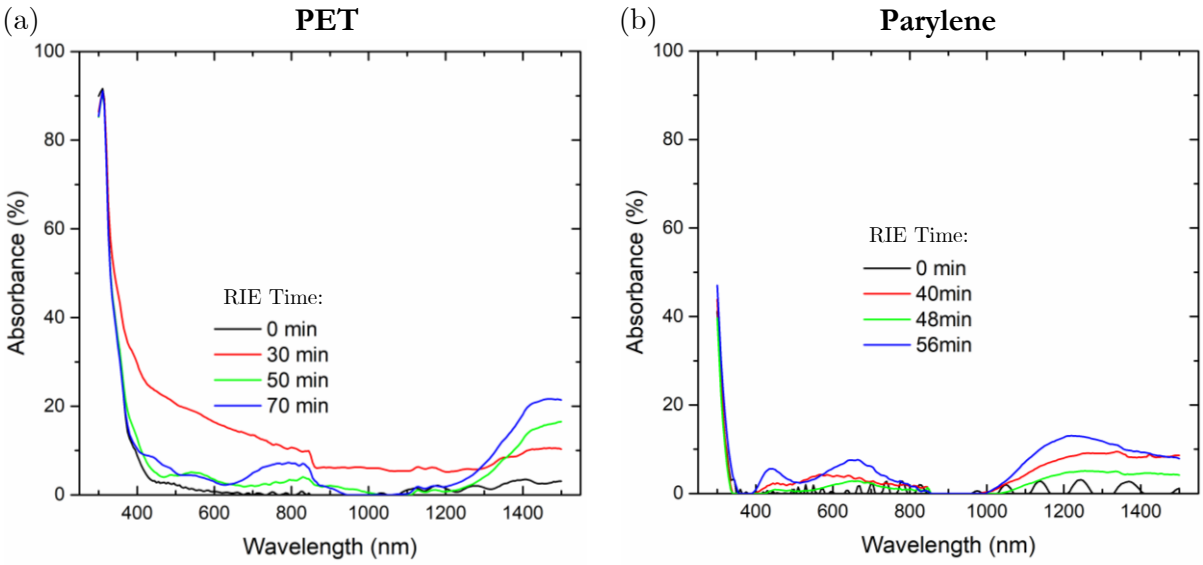

Figure 3.7.4 – Absorbance spectra of (a) PET and (b) parylene surfaces with varying SF_6 plasma treatment time. (SF_6 50sccm, 50W)

The peaks shown in 1400 nm and 800 nm for PET and 1200 nm and 650nm for parylene are thought to be related to the periodicity effect. The peaks below 400 nm are due to high UV absorption of these polymeric materials. In Table 3.7.1 are shown the calculated average values of the previously mentioned spectra. This was accomplished by integrating the spectra from 400 nm to 1400 nm.

Table 3.7.1 – Calculated average transmittance, haze, reflectance and absorbance.

	PET			Parylene		
	30min	50min	70min	40min	48min	56min
Avg. Total Trans. (%)	76.4	80.0	77.9	79.7	80.6	72.8
Avg. Diffuse Trans (%)	44.7	67.2	64.2	50.7	49.1	56.9
Avg. Haze (%)	59.6	83.8	82.6	62.8	60.6	77.0
Avg. Total Refl. (%)	12.7	16.9	17.7	16.6	17.7	21.9
Avg. Absorbance (%)	10.8	3.1	4.4	3.8	1.9	5.5

The comparison shown in Table 3.7.1 suggests that the application of plasma treatment, both on PET (and the use of 1.6 μm PS spheres) and parylene (and the use of 1.6 μm) is a good approach for photonic application. Nevertheless, the scattering effect, characterized by the haze average value, is higher in PET (83% against 77%). The average total transmittance of PET and parylene is similar. However, it is worth noting that losses occur in the parylene-glass interface, as well as in the backside of the glass and the glass itself. It is presented, in Figure C 5, a CF_4 plasma-treated PET sample which demonstrates extremely high transmittance and haze. Contrary to what has been observed in SF_6 and O_2/SF_6 plasma treated surfaces, the periodicity effect is less significant.

3.8 Solar Cell Measurements

This section focuses on analyzing the optical benefits provided by the photonic-structured parylene on test devices. For that, two a-Si:H solar cell architectures were tested. First, a superstrate (p-i-n) configuration with 4.91 mm^2 cells' area, and second a substrate configuration (n-i-p) with an active area of 20.2 mm^2. It is worth mentioning that the first configuration is not preferential, due to the existence of a glass layer. The best conditions were provided by the substrate type layer configuration, where the parylene layer was deposited directly onto the cells front side, not on the glass, in order for such layer to be integrated as close as possible to the cells' absorber layer and, therefore, allow pronounced light trapping effects.

The cells in superstrate configuration were initially characterized without any coating (the "reference"). Then, a 5 μm flat coating of parylene was deposited onto the cells' front side, i.e. on its 3 mm thick regular glass substrate ("smooth parylene"), as sketched in Figure 3.8.1. Finally, the parylene was patterned with 1.6 μm masking PS spheres and 10 minutes of O_2 plasma treatment followed by 1 minute SF_6 plasma treatment ("textured parylene"). The I-V curves of a solar cell before and after such patterning are shown in Figure 3.8.1.

Table 3.8.1 – Main parameters obtained from the I-V curves: Short-circuit current density, open-circuit voltage, fill factor and efficiency, respectively.

	Ref.	Smooth	Textured
J_{SC} (mA/cm^2)	15.01	14.76	15.10
V_{OC} (V)	0.91	0.90	0.90
FF (%)	54.98	55.50	55.64
Efficiency (%)	7.49	7.40	7.54

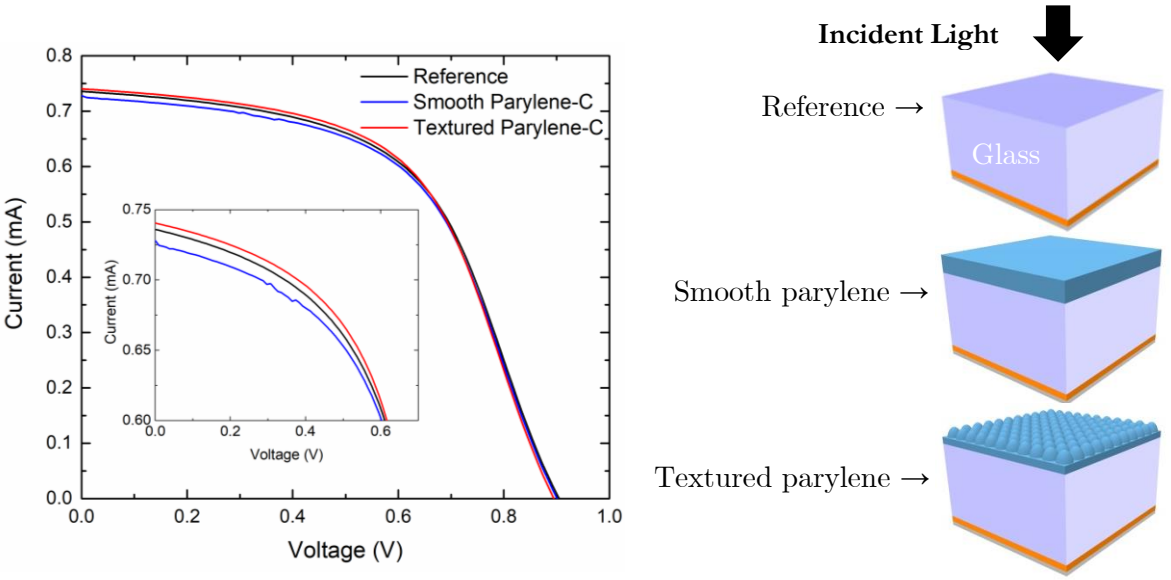

Figure 3.8.1 – Comparison between measured I-V curves of a solar cell without any coating (reference), with a flat 5 µm parylene coating (smooth) and after structuring the parylene (textured). The inset shows an amplified view of the I-V curves between 0V and 0.7V.

Though the difference between the three I-V curves is small, it is possible to verify the current loss from the reference relative to the smooth parylene measurements (Figure C 6). This loss is to be expected, due to the addition of a front material with a higher refractive index (~1.64) than that of glass (~1.5), through which light has to travel. Thus, a lower efficiency is also registered. However, when adding the scattering action of the photonic features, the textured parylene cell revealed an increase both in J_{SC} and efficiency.

Comparing the values of efficiency and J_{SC} enhancement presented in Figure 3.8.2, the texturing of parylene causes an average increase of 0.39% and 0.05% in J_{SC} and efficiency, respectively, relative to the smooth parylene coated cells. Therefore, the slight enhancement on the electrical performance of the tested cells implies that the light scattering effect produced by the developed coating exceeds the reduction of total transmittance observed in section 3.7. It also reveals that this coating should cause a significant efficiency increase if applied directly on the cell's surface, instead of on glass.

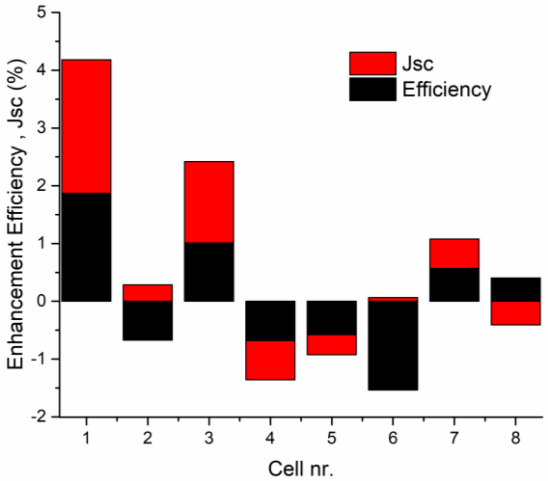

Figure 3.8.2 – J_{SC} and efficiency enhancement of textured parylene coated cells relative to flat ones.

Table C 3 and Table C 4 show the detailed electrical performance enhancement of the cells with, respectively, smooth parylene relative to the reference, and textured parylene relative to smooth parylene.

In view of the above, a better implementation is expected when the parylene is deposited directly on the cell layer with a substrate configuration (as sketched in Figure 3.8.3). This was performed in the second batch of cells, which revealed much more pronounced photocurrent (J_{SC}) enhancements with the addition of the textured parylene.

The spectral contributions to such photocurrent can be analyzed with the EQE spectra of the cells plotted in Figure 3.8.3.

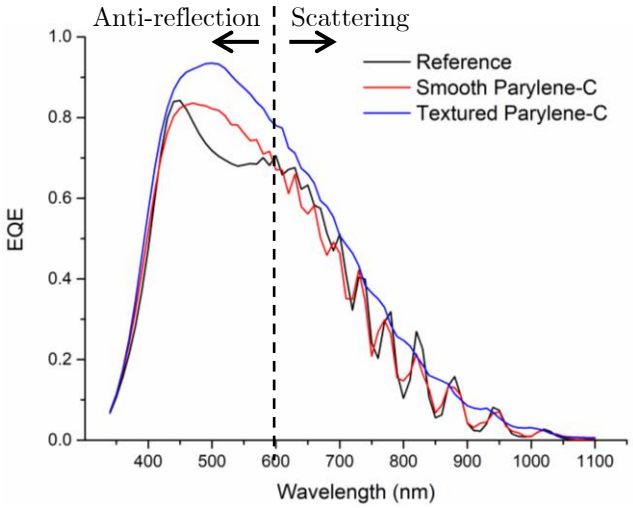

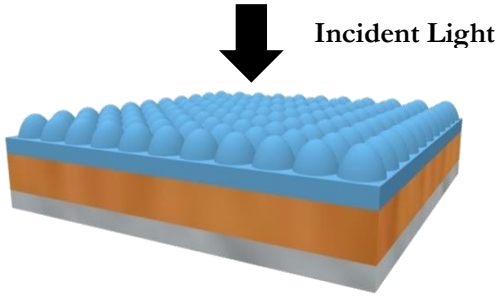

Table 3.8.2 – Photocurrent values of a a-Si n-i-p solar cell.

	Reference	Smooth	Textured
J_{SC} (mA/cm^2)	16.3	16.6	19.2

Figure 3.8.3 – Comparison between EQE measurements (Left) of a-Si solar cells with the same coatings as those of Figure 3.8.1, but with a substrate (n-i-p) configuration. (Right)

In this case, the results reveal that the parylene layer directly deposited onto the cells' surface generates an anti-reflection effect, characterized by the increase in EQE in the UV-Visible (<600nm wavelengths) region of the spectrum. This effect enables an increase in J_{SC} of 1.7% relative to the reference. After the parylene surface was textured, not only the anti-reflection effect rose, but also a very pronounced light scattering effect was registered, contributing to the enhanced EQE at red-NIR wavelengths (>600nm). Furthermore, the scattering effect smoothed the interference peaks on the right side of the dashed line in Figure 3.8.3, due to the redirection of the vertically-incident light towards a range of other forward-scattered directions. [29] These photonic properties enabled a notorious J_{SC} increase up to ~15.9% relative to the unpatterned flat parylene. In Figure 3.8.4 is represented the J_{SC} enhancement for the studied batch of n-i-p cells.

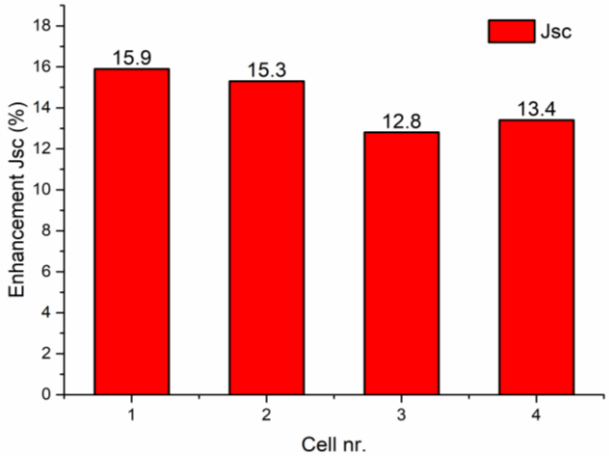

Figure 3.8.4 – J_{SC} enhancement of the studied batch of cells with a substrate (n-i-p) configuration.

4 Conclusions and Future Perspectives

Superhydrophobic surfaces with extreme light scattering capability were herein developed and optimized through the use of a colloidal lithography (CL) patterning method. The first stage of CL consisted in the deposition of a hexagonal compact self-assembled monolayer of polystyrene (PS) microspheres onto a material's surface. These PS monolayers were then successfully used as hard mask in the patterning of different materials' surfaces through reactive ion etching (RIE). The use of different types of plasmas in the RIE stage allowed the control of the etching rate and thus, the precision of the process.

The comparison between sphere sizes pointed out that 1.6 μm PS spheres arrange in a practically perfect array (see appendix C), whereas 1.3 μm PS spheres do not. Indeed, the latter colloids form "crystalline" zones where the assembly is very good; nonetheless the monolayer is mainly composed of disorganized spheres. Regarding hydrophobicity, this characteristic should decrease the roughness factor and the fraction of solid-liquid contact interface, defined in section 1.2, contributing to the decrease of the surface hydrophobicity.

The RIE treatment produced cylindrical/dome-like shaped structures. At the same time, the application of plasma on the surface produces a functionalization effect. This effect enables the modification of a given surface's wettability by the introduction of hydrophilic or hydrophobic functional groups. The tuning of these two factors (surface roughness and chemistry) produced highly hydrophobic surfaces with impressive static contact water angles up to 140° and 167° on PET and parylene, respectively. However, PET revealed a high contact angle (CA) hysteresis (~50°). The extreme adhesive behavior of PET can be related to the petal effect (High CA with high CA hysteresis), thus it is disadvantageous for the intended (super)hydrophobic self-cleaning effect. Nevertheless, its properties are very promising in the anti-fogging field. This suggests that droplets always remained in Wenzel state. Contrasting with these properties, parylene showed very high CA and very low hysteresis. Treated parylene was thus rendered superhydrophobic.

The COS treatment was tested on parylene surfaces, both with masking PS spheres and without them. It was observed that the samples patterned without spheres presented superhydrophobic static CA (~150°), however they cannot provide the water roll-off effect needed for self-cleaning applications, due to pinning effects and low surface homogeneity. On the other hand, parylene surfaces patterned with CL showed extremely high static CA (~162°), while presenting very low CA hysteresis (10°), thus providing the roll-off effect.

An analytical comparison between experimental CA measurements and both Wenzel and Cassie-Baxter models determined that surface chemistry has a crucial role in tuning wettability properties. That was verified by the dissimilarities between the models and experimental results. It was further found that these dissimilarities were more significant for PET surfaces, indicating the enhancement due to chemistry alteration would change significantly over RIE time. The highest enhancement was 74% and 25% comparing with Wenzel and Cassie-Baxter, respectively. For plasma-treated parylene, the CA enhancement from chemistry modification had little deviation with increasing RIE time and was calculated

to be 45% and 15% comparing with Wenzel and Cassie-Baxter, respectively. X-ray photoelectron spectrophotometry (XPS) analysis verified the changes in surface chemistry and further confirmed the functionalization by the plasma process gas.

In what concerns the optical properties of the patterned front structures, it was observed that plasma treatment causes a slight decrease in transmittance and consequently a slight increase in reflectance. This effect was due to the samples' "whitening" derived from the plasma treatment. The use of different PS sphere sizes influences the positioning of localized depressions in transmittance and of localized peaks in reflectance corresponding to wavelengths of the same order as the spheres' pitch. Average diffuse transmittance increased from 5% and 2% (on PET and parylene, respectively) to values over 60%. This corresponds to average haze in transmittance (equation 1.4) of over 80% on PET and 70% on parylene. In some wavelength ranges (as shown in Figure 3.7.3), haze spectra reaches almost the maximum value of ~98%. It is worth noting that PET surfaces treated with 100W SF_6 plasma had their total transmittance remarkably surpassing the untreated transmittance at ~1100 nm (Figure C 4).

A preliminary test of the application of parylene was performed on the glass surface of an a-Si solar cell with a superstrate configuration. The addition of a flat parylene layer caused an average loss in J_{SC} and efficiency of 1.04% and 0.99%, respectively. However, the texturing of parylene resulted in an enhancement of 0.39% and 0.05% in J_{SC} and efficiency, respectively, relative to smooth parylene coated cells. It is important to emphasize the enhancement observed with the parylene patterning even though there was a 3mm glass layer separating the coating from the actual solar cells. The application of a flat parylene coating directly on the cell's illuminated surface enabled a 1.7% increase of J_{SC} relative to the uncoated reference cell and the subsequent patterning provided an average enhancement of 15.9% relative to the that with unpatterned flat parylene. This impressive result is the proof of concept and opens the door for application of low-cost, self-cleaning, photonic coatings in thin film PV.

4.1 Remarks for near-future work

Etching of glass was not achieved due to the low selectivity of the available gases on the RIE system. A study [36] has reported the successful etching of glass with CHF3, also with PS microspheres masking. PS microspheres deposition can be further improved which would provide increased consistency throughout the process, as the subsequent pattern should have a direct impact on both wetting and optical properties. However, this study was not able to verify that impact. The measurement and control of selectivity during RIE treatment is extremely important and should be thoroughly investigated, since it has a direct impact on aspect ratio. It would be interesting to study the use of different sized PS spheres. Also the use of silica microspheres (which present higher resistance to plasma treatment than PS) could enable the fabrication of higher structures without significant loss in diameter.

References

[1] M. Simon and E. L. Meyer, "Detection and analysis of hot-spot formation in solar cells," *Sol. Energy Mater. Sol. Cells*, vol. 94, no. 2, pp. 106–113, 2010.

[2] O. Sanchez-sobrado *et al.*, "Colloidal-lithographed TiO2 photonic nanostructures for solar cell light trapping," *Mater. Chem. C*, pp. 6852–6861, 2017.

[3] M. Reza, H. Hizam, C. Gomes, M. Amran, M. Ismael, and S. Hajighorbani, "Power loss due to soiling on solar panel : A review," *Renew. Sustain. Energy Rev.*, vol. 59, pp. 1307–1316, 2016.

[4] R. Karmouch and H. EL Hor, "Solar Cells Performance Reduction under the Effect of Dust in Jazan Region," *J. Fundam. Renew. Energy Appl.*, vol. 7, no. 2, pp. 1–4, 2017.

[5] H. Pedersen, J. Strauss, and J. Selj, "Effect of soiling on photovoltaic modules in Norway," *Energy Procedia*, vol. 92, no. 1876, pp. 585–589, 2016.

[6] A. M. Pavan, A. Mellit, and D. De Pieri, "The effect of soiling on energy production for large-scale photovoltaic plants," *Sol. Energy*, vol. 85, no. 5, pp. 1128–1136, 2011.

[7] S. A. Kalogirou, R. Agathokleous, and G. Panayiotou, "On-site PV characterization and the effect of soiling on their performance," *Energy*, vol. 51, pp. 439–446, 2013.

[8] H. Qasem, "Effect of accumulated dust on the performance of photovoltaic modules," 2013.

[9] A. Y. Al-Hasan, "A new correlation for direct beam solar radiation received by photovoltaic panel with sand dust accumulated on its surface," *Sol. Energy*, vol. 63, no. 5, pp. 323–333, 1998.

[10] A. Sya, A. K. Pandey, N. N. Adzman, and N. Abd, "Advances in approaches and methods for self-cleaning of solar photovoltaic panels," *Sol. Energy*, vol. 162, no. 2018, pp. 597–619, 2018.

[11] A. Peter Amalathas and M. Alkaisi, "Upright nanopyramid structured cover glass with light harvesting and self-cleaning effects for solar cell applications," *J. Phys. D. Appl. Phys.*, vol. 49, p. 465601, 2016.

[12] P.-G. de Gennes, F. Brochard-Wyart, and D. Quéré, *Capillarity and Wetting Phenomena*. 2004.

[13] Y. Yuan and T. R. Lee, *Contact Angle and Wetting Properties*. 2013.

[14] R. P. Woodward, "Contact Angle Measurements Using the Drop Shape Method," pp. 1–8.

[15] R. E. JOHNSON and R. H. DETTRE, "Contact Angle Hysteresis - Study of an Idealized Rough Surface," in *Contact Angle, Wettability, and Adhesion*, pp. 112–135.

[16] R. N. Wenzel, "RESISTANCE OF SOLID SURFACES TO WETTING BY WATER," *Ind. Eng. Chem.*, vol. 28, no. 8, pp. 988–994, 1936.

[17] B. Bhushan and M. Nosonovsky, "The rose petal effect and the modes of superhydrophobicity," pp. 4713–4728, 2010.

[18] A. B. D. Cassie and S. Baxter, "Wettability of porous surfaces," *Trans. Faraday Soc.*, vol. 40, no. 0, pp. 546–551, 1944.

[19] S. Wang and L. Jiang, "Definition of Superhydrophobic States," *Adv. Mater.*, vol. 19, pp. 3423–3424, 2007.

[20] K. Liu, X. Yao, and L. Jiang, "Recent developments in bio-inspired special

wettability," *Chem. Soc. Rev.*, vol. 39, no. 8, pp. 3240–3255, 2010.

[21] T. Verho *et al.*, "Reversible switching between superhydrophobic states on a hierarchically structured surface," *Proc. Natl. Acad. Sci.*, vol. 109, no. 26, p. 10210 LP-10213, Jun. 2012.

[22] X. Bi, B. P. Crum, and W. Li, "Super Hydrophobic Parylene-C Produced by Consecutive O 2 and SF 6 Plasma Treatment," vol. 23, no. 3, pp. 628–635, 2014.

[23] L. Schneider, M. Laustsen, N. Mandsberg, and R. Taboryski, "The Influence of Structure Heights and Opening Angles of Micro- and Nanocones on the Macroscopic Surface Wetting Properties," *Sci. Rep.*, no. September 2015, pp. 1–9, 2016.

[24] M. Resnik, R. Zaplotnik, M. Mozetic, and A. Vesel, "Comparison of SF6 and CF4 Plasma Treatment for Surface Hydrophobization of PET Polymer," 2018.

[25] M. Golda, M. Brzychczy-Wloch, M. Faryna, K. Engvall, and A. Kotarba, "Oxygen plasma functionalization of parylene C coating for implants surface : Nanotopography and active sites for drug anchoring," vol. 33, pp. 4221–4227, 2013.

[26] N. Barthlott, Wilhelm; Ehler, "Raster-Elektronenmikroskopie der Epidermis-Oberflächen von Spermatophyten," *Trop. und Subtrop. Pflanzenwelt*, vol. 19, p. 110, 1977.

[27] W. Barthlott and C. Neinhuis, "Purity of the sacred lotus , or escape from contamination in biological surfaces," *Planta*, vol. 202, no. 1, pp. 1–8, 1996.

[28] M. Jin *et al.*, "Superhydrophobic Aligned Polystyrene Nanotube Films with High Adhesive Force," *Adv. Mater.*, vol. 17, no. 16, pp. 1977–1981.

[29] M. J. Mendes *et al.*, "Design of optimized wave-optical spheroidal nanostructures for photonic-enhanced solar cells," *Nano Energy*, vol. 26, pp. 286–296, 2016.

[30] I. Martins, "Parylene C as substrate , dielectric and encapsulation for flexible electronics applications," FCT UNL, 2017.

[31] I. Langmuir, "THE CONSTITUTION AND FUNDAMENTAL PROPERTIES OF SOLIDS AND LIQUIDS. II. LIQUIDS.1," *J. Am. Chem. Soc.*, vol. 39, no. 9, pp. 1848–1906, 1917.

[32] K. B. Blodgett, "Films Built by Depositing Successive Monomolecular Layers on a Solid Surface," *J. Am. Chem. Soc.*, vol. 57, no. 6, pp. 1007–1022, 1935.

[33] A. Emoto, E. Uchida, and T. Fukuda, "Fabrication and optical properties of binary colloidal crystal monolayers consisting of micro- and nano-polystyrene spheres," *Colloids Surfaces A Physicochem. Eng. Asp.*, vol. 396, pp. 189–194, 2012.

[34] H. Sharifi and G. Gardner, "Plasma RIE Etching Fundamentals and Applications," 2008.

[35] J. T. C. Yeh and K. R. Grebe, "Patterning of polyparaxylylenes by reactive ion etching," vol. 604, no. 1983, 2014.

[36] E. Baquedano, P. A. Postigo, P. Caño, and L. Torné, "Increased Efficiency of Solar Cells Protected by Hydrophobic and Hydrophilic Anti-Reflecting Nanostructured Glasses," 2017.

Appendix A

In this appendix will be provided additional information regarding the Introduction section, that could not be incorporated in the main text, either for lack of space or due to its detail character.

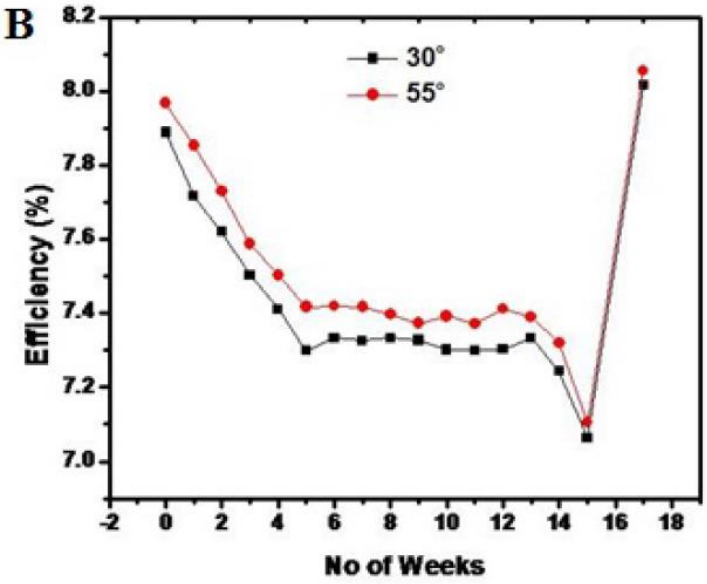

Figure A 1 – Decreasing efficiency of two solar panels tilted at 30° and 55° over 16 weeks, due to dust deposition in the Jazan Region and reposition of efficiency by surface cleaning. (reproduced from ref.[4]*)*

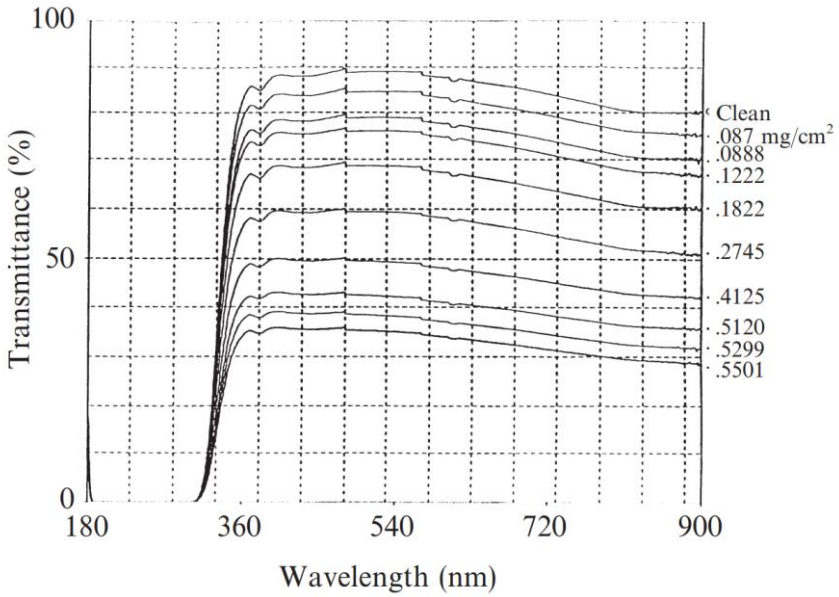

Figure A 2 – Spectral transmittance of light through glass with different sand dust amounts. (reproduced from ref.[9]*)*

Figure A 3 correlates the decreasing roughness of a wax substrate through the application of successive heat treatments with advancing and receding contact angles.

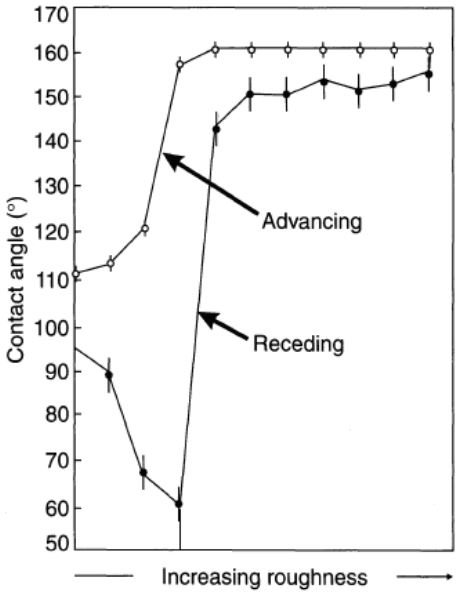

Figure A 3 – ACA and RCA on successively heat treated wax. (Reproduced from ref.[12]*)*

(a) (b)

Figure A 4 - Nelumbo nucifera leaf http://plantinfo.co.za/plant/nelumbo-nucifera/(a) and respective SEM image [27] *(b) Bar=20 µm*

(a) (b)

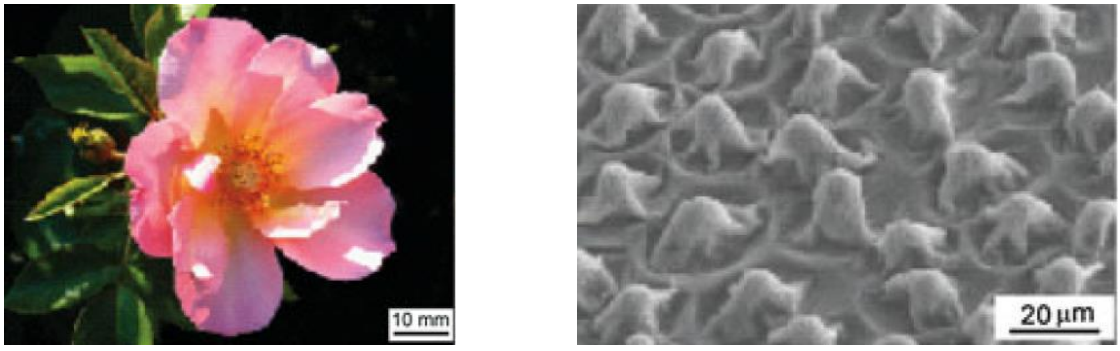

Figure A 5 – Rose petal (a) and respective SEM image [27] *(b)*

Table A 1 summarizes the general influence of the parameters used in the reactive ion etching process.

Table A 1 – Reactive Ion Etching parameters influence.

	Gas Flow (sccm)	**RF Power (W)**	**Pressure (mTorr)**
Increase etch rate	Increase	Increase	Increase
Increase etch anisotropy	-	Increase	Decrease
Increase selectivity	-	Decrease	Increase

Appendix B

In this appendix will be provided additional information regarding the Materials and Methods section, that could not be incorporated in the main text, either for lack of space or due to its detail character.

Figure B 1 presents the calibration of the parylene-C deposition.

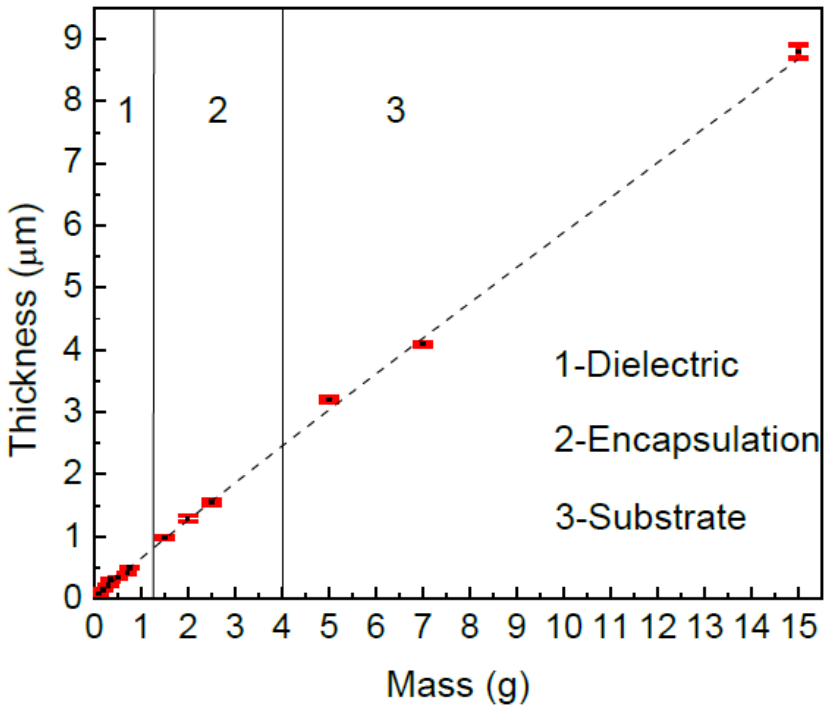

Figure B 1 - Calibration of the parylene deposition system. Relation between the dimer mass and the parylene film thickness (Reproduced from ref.[30]*)*

Figure B 2 illustrates the chemical stages of the deposition of parylene-C.

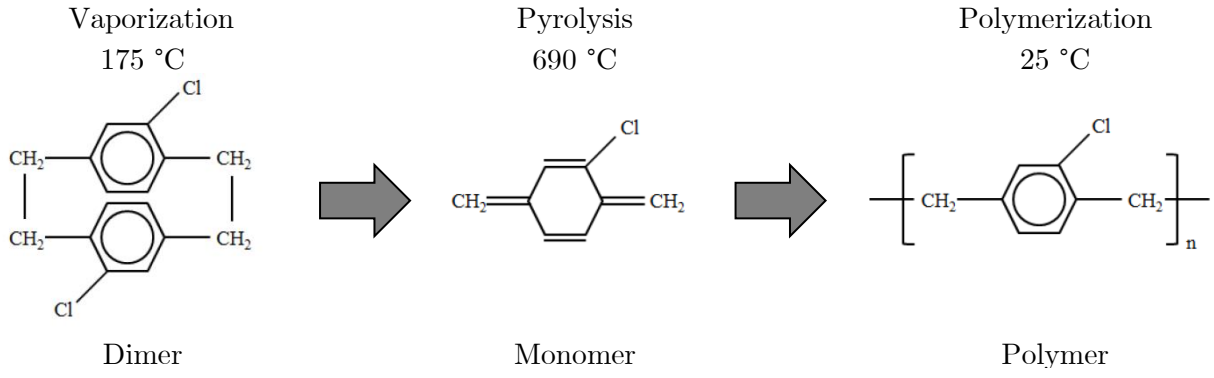

Figure B 2 – Parylene-C deposition stages.

Appendix C

In this appendix will be provided additional information regarding the Results and Discussion section, that could not be incorporated in the main text, either for lack of space or due to its detail character.

Figure C 1 shows a high resolution SEM image of a 1.6 μm polystyrene deposition demonstrating the excellent self-assembly property of these spheres over large areas.

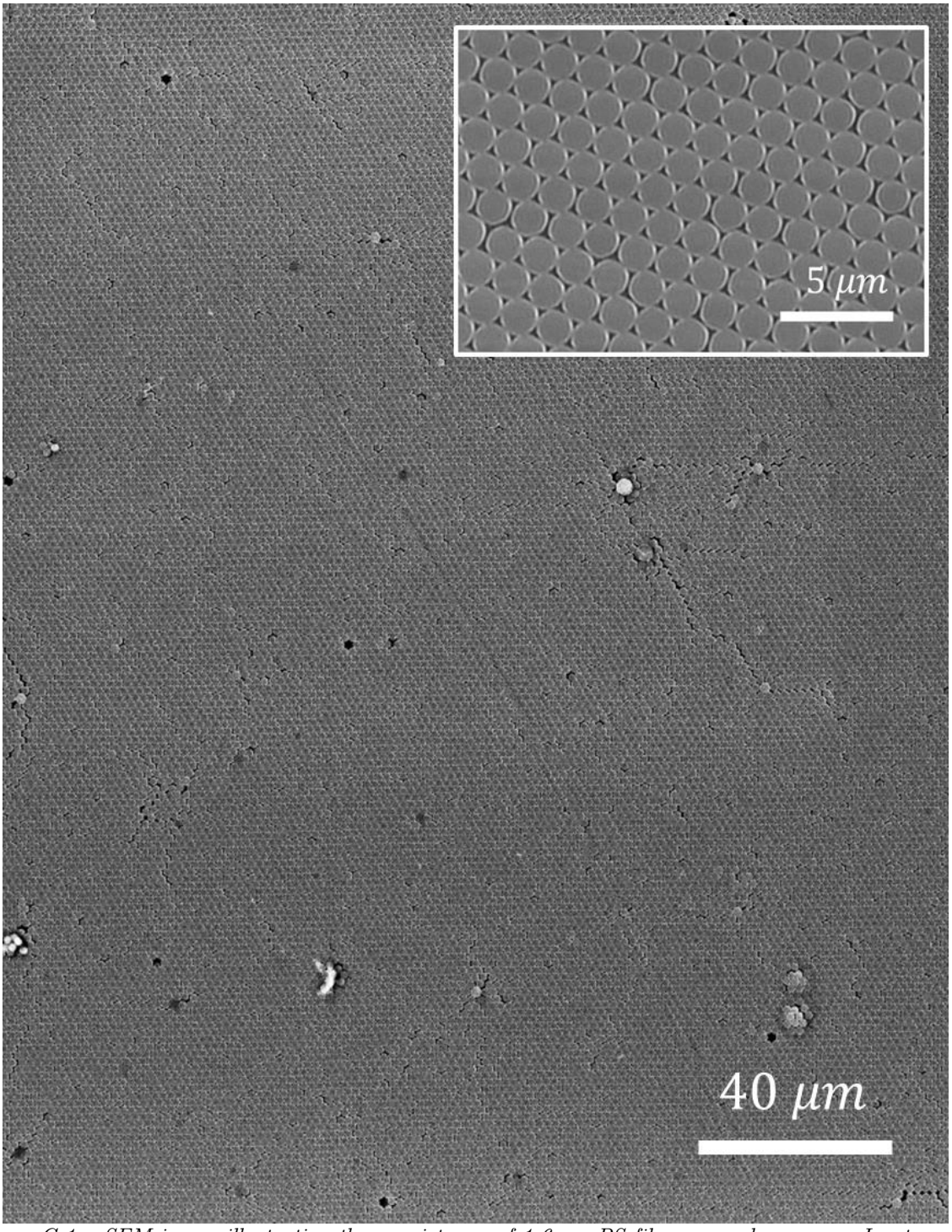

Figure C 1 – SEM image illustrating the consistency of 1.6 μm PS film over a large area. Inset showing a magnified, perfectly arranged region.

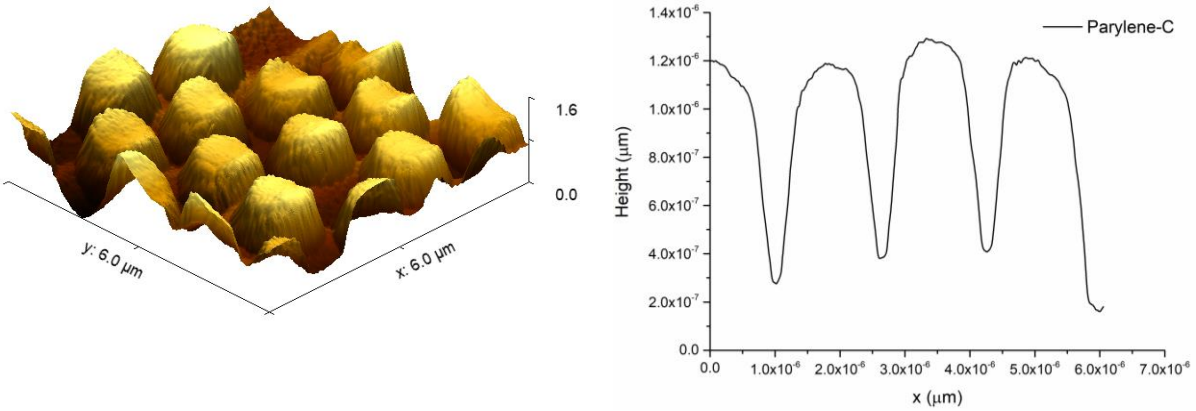

Figure C 2 - (a) AFM 3D image of 70min etched parylene-C with 1.6 µm PS spheres (50W, O_2/SF_6 – 50sccm) and (b) respective AFM cross section profile.

Table C 1 provides a detailed list of the positions and full-width-half-maximum (FWHM) values of the detected peaks in the XPS analysis.

Table C 1 – Detected functional groups from C 1s spectra deconvolution on (a) untreated parylene, (b) O_2 plasma-treated parylene and (c) O_2-SF_6 plasma treatment.

	Untreated		**O_2 Plasma**		**O_2/SF_6 Plasma**	
	Position	FWHM	Position	FWHM	Position	FWHM
C-C	284.80	0.92	284.79	1.1	284.8	1.08
C-Cl	285.86	0.92	285.84	1.1	285.86	1.08
C=O	-	-	286.87	1.1	286.88	1.1
O-C=O	-	-	287.92	1.1	287.93	1.1
CO3	-	-	291.51	1.1	291.53	1.1
CF	-	-	289.15	1.1	289.17	1.1
CF_2	-	-	290.14	1.1	290.14	1.1
CF_3	-	-	-	-	293.69	1.1

Figure C 3 shows the dynamic CA of parylene treated with SF_6 plasma in RIE, demonstrating alternative conditions to achieve superhydrophobicity.

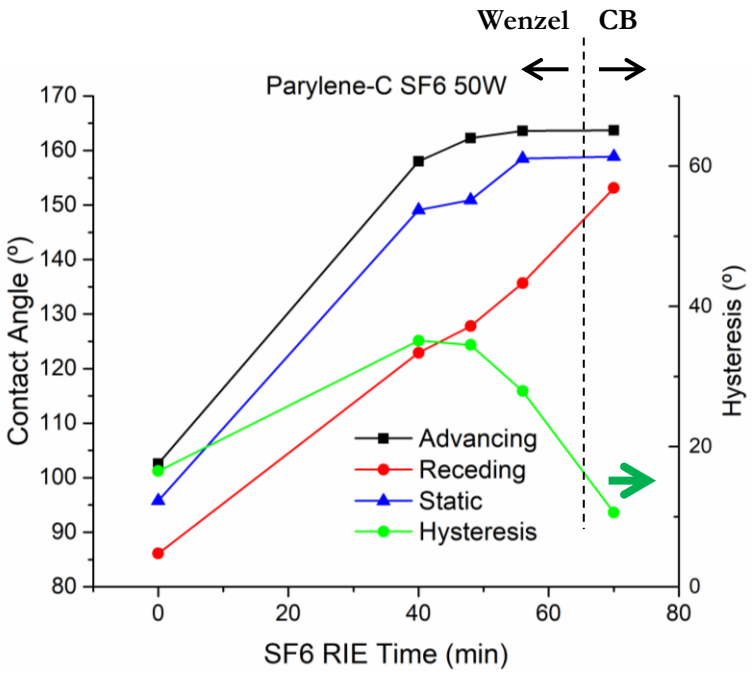

Figure C 3 – Dyamic CA of parylene-C treated with SF_6 plasma (50W, 50 sccm) masked with 1.3 µm PS spheres.

Table C 2 – Parameters for the calculation of CA through both Wenzel and Cassie-Baxter models.

Time (min)	PET 1.6 SF_6 50W 50sccm			Parylene-C 1.3 SF_6 50W 50sccm		
	30	50	70	40	56	70
D_{PS}	1.6	1.6	1.6	1.3	1.3	1.3
d_{avg}	1.28	1.14	0.92	1.00	0.90	0.79
h_{avg}	0.92	1.46	2.15	0.64	1.03	1.26
SCA, θ	87.4	87.4	87.4	95.8	95.8	95.8
n_1	10000	10000	10000	10000	10000	10000
n_2	10000	10000	10000	10000	10000	10000
R_f	2.67	3.37	3.80	2.37	2.98	3.13
Wenzel	82.9	80.9	80.1	103.9	107.5	108.5
Cassie-Baxter	103.9	114.2	130.4	126.4	134.2	140.5
Experimental	129.6	137.1	139.7	149.1	158.5	158.9

Figure C 4 and Figure C 5 show transmittance and haze in transmittance spectra of respectively, a PET sample treated with SF_6 that exceeds the original transmittance value at ~1100nm and a PET sample treated with CF_4 that presents very good total transmittance after RIE and an exceptional diffuse transmittance.

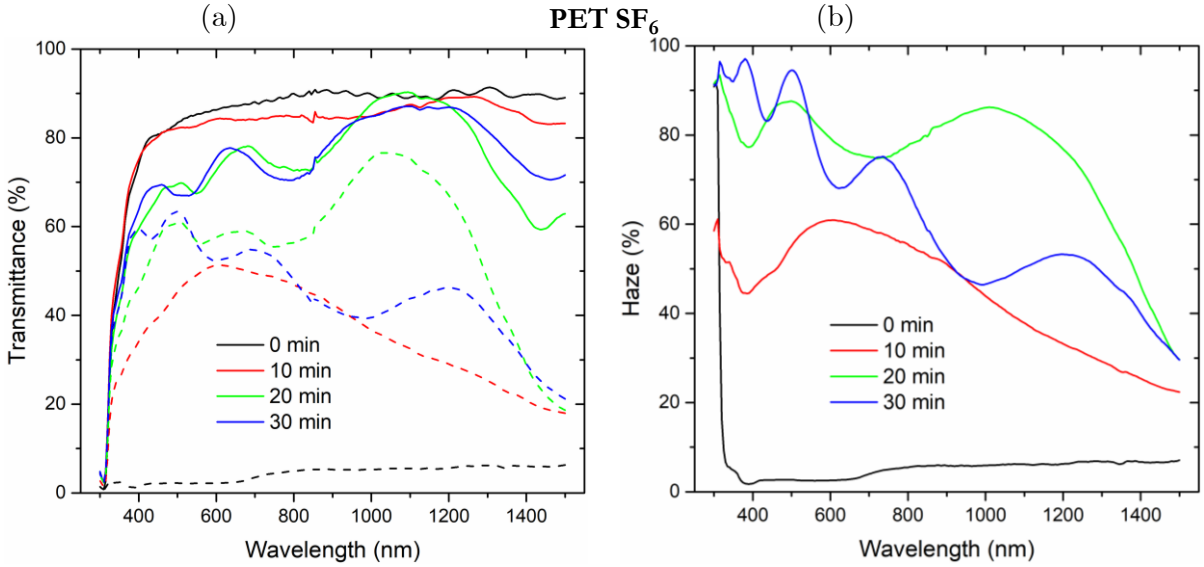

Figure C 4 – (a) Total (solid lines) and diffuse (dashed lines) transmittance and (b) haze spectra of PET surfaces with varying RIE time. The surface was treated with 100W

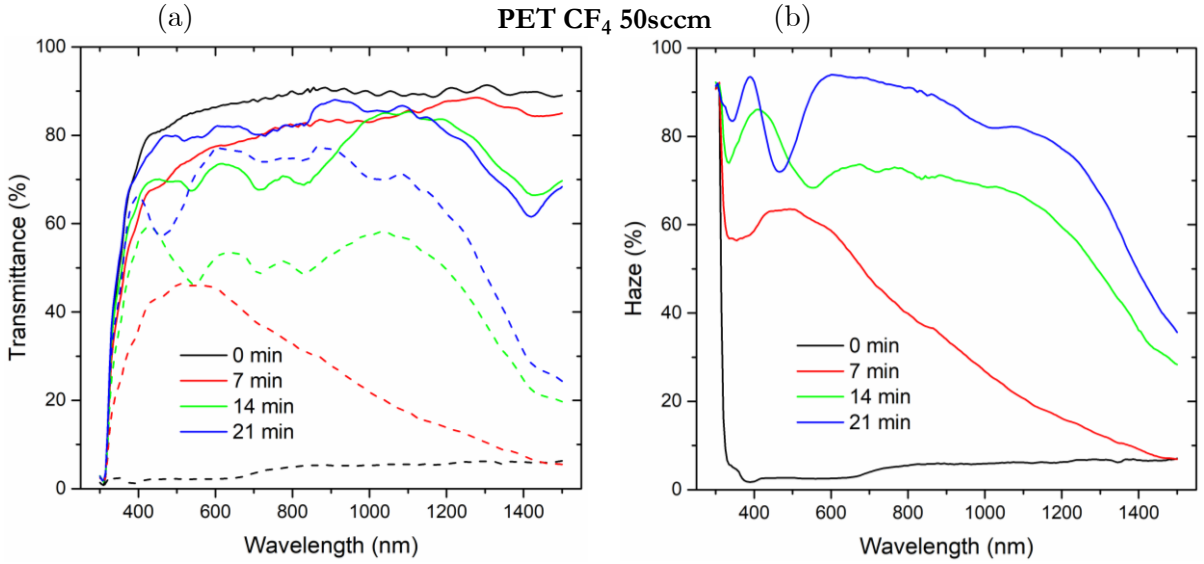

Figure C 5 – (a) Total (solid lines) and diffuse (dashed lines) transmittance and (b) haze spectra of PET surfaces with varying RIE time. The surface was treated with CF_4 50sccm, 100W

Table C 3 and Table C 4 present detailed information regarding the enhancement of the main parameters extracted from the I-V curves from coating the cells with smooth parylene and after RIE treatment, respectively.

Table C 3 – Enhancement of parylene-C coated solar cells relative to reference solar cells.

Cell nr.	V_{OC}	J_{SC}	FF	$Efficiency$
1	-0.41237	-1.67653	0.942166	-1.16051
2	-0.32123	-1.49765	1.122031	-0.71339
3	-0.55656	-1.46732	0.746184	-1.28405
4	-0.7124	-1.0237	0.708996	-1.03221
5	-0.56885	-0.72663	0.841132	-0.4609
6	-0.65387	-0.85756	0.619895	-0.89439
7	-0.38797	-0.52842	0.561044	-0.35742
8	-1.68599	-0.55351	0.255267	-1.98097

Table C 4 – Enhancement of textured parylene-C coated solar cells relative to smooth parylene coated solar cells.

Cell nr.	V_{OC}	J_{SC}	FF	$Efficiency$
1	-0.68257	2.311006	0.254245	1.871318
2	0.232552	0.2838	-1.18504	-0.67353
3	0.096699	1.407327	-0.48792	1.009541
4	0.247574	-0.67745	-0.24968	-0.68007
5	-0.29107	-0.34666	0.059565	-0.57725
6	-0.66519	0.066787	-0.94378	-1.53714
7	0.010024	0.506751	0.053859	0.570474
8	0.471791	-0.40634	0.341312	0.404752

Figure C 6 illustrates the data from Table C 3, regarding efficiency and J_{SC}. As expected, the addition of a flat layer of parylene decreases these parameters.

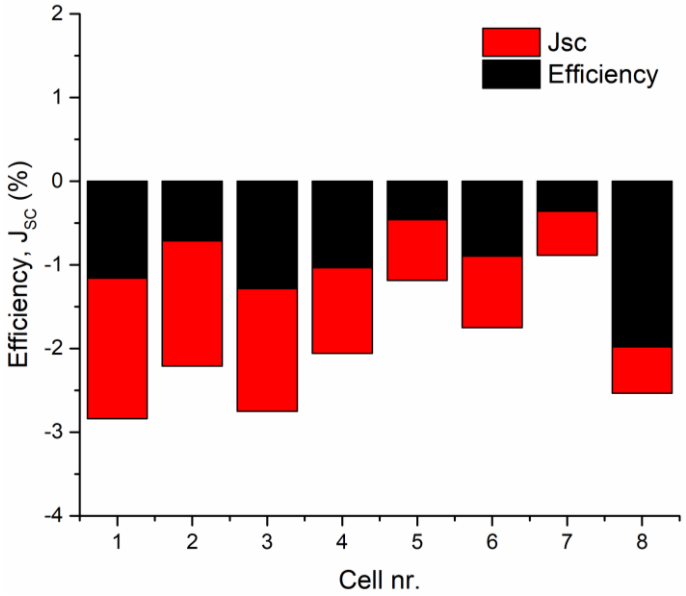

Figure C 6 – Cells' efficiency and J_{SC} loss by adding a parylene smooth layer.

Figure C 7 shows SEM images of superior resolution of top and cross sectional views of a PET surface with 30 minutes SF_6 100W

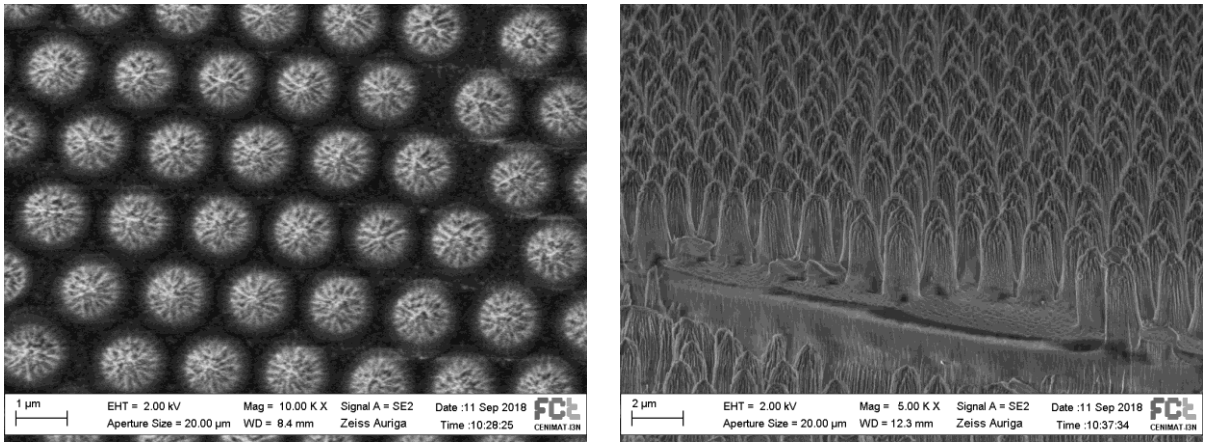

Figure C 7 – Top and cross sectional images of a PET surface with 30 minutes SF_6 100W.